Available online at www.sciencedirect.com
ScienceDirect
Journal of Sound and Vibration 306 (2007) 31–58
JOURNAL OF SOUND AND VIBRATION
www.elsevier.com/locate/jsvi

Green's functions for analysis of dynamic response of wheel/rail to vertical excitation

Traian Mazilu*

Department of Railway Vehicles, University Politehnica of Bucharest, Splaiul Independentei, 313, Bucharest 060032, Romania

Received 1 February 2007; received in revised form 6 May 2007; accepted 26 May 2007

Abstract

An analytical model to simulate wheel/rail interaction using the Green's functions method is proposed in this paper. The model consists of a moving wheel on a discretely supported rail. Particularly for this model of rail, the bending and the longitudinal displacement are coupled due to the rail pad and a complex model of the rail pad is adopted. An efficient method for solving a time-domain analysis for wheel/rail interaction is presented. The method is based on the properties of the rail's Green functions and starting to these functions, a track's Green matrix is assembled for the numerical simulations of wheel/rail response due to three kinds of vertical excitations: the steady-state interaction, the rail corrugation and the wheel flat. The study points to influence of the worn rail—rigid contact—on variation in the wheel/rail contact force. The concept of pinned–pinned inhibitive rail pad is also presented.

1. Introduction

When a wheel rolls along a rail, both are set in vertical vibration by the irregularities (roughness, waviness) of the running surfaces, or by discontinuities of the rail and wheel such as turnouts, crossings, rail joints and wheel flats. Even geometrically perfect surfaces may generate vibration due to varying dynamic stiffness of a track within a sleeper bay. The study of vibration generated by a rolling wheel on a rail is critical in predicting the short-pitch rail corrugation and wheel–rail noise.

The issue of the wheel–rail vibration system may be solved by frequency-domain analysis and time-domain analysis. Frequency-domain analysis uses a mathematical transformation which aims to find harmonic solutions for the complicated motion equations. Thus, the receptance or the impedance at different frequencies is calculated. Remington [1] and Thompson [2] used the impedance and the receptance respectively, of a Bernoulli–Euler beam on an elastic foundation. The receptance of an Euler beam on a layer of intermediate masses and the receptance of a double Euler beam system on elastic support were calculated by Sato [3]. Grassie et al. [4] have systematically studied the rail's dynamic response using both the Euler beam theory and the Timoshenko beam theory (with shear deformation and rotational inertia). Frequency-domain analysis is the starting point in rolling noise prediction, according to Remington [5] and Thompson [6].

*Tel.: +40 724230091; fax: +40 213409238.
E-mail address: trmazilu@yahoo.com

0022-460X/$ - see front matter © 2007 Elsevier Ltd. All rights reserved.
doi:10.1016/j.jsv.2007.05.037

Time-domain analysis for the wheel/rail response is based often on the track linear model. In many analytical approaches, the track's equations of motions are first decoupled by the modal analysis and then the modal superposition technique is applied in order to calculate the track response. If the track is regarded as a linear finite element model, the response is obtained by the modal analysis, as well. Clark et al. [7] have developed a track dynamic and wheel/rail interaction model, considering a 20-sleeper long discretely supported model. The dynamic behaviour of a track presenting rail corrugation has been studied. An advanced track model based on the finite element method has been developed by Nielsen and Igeland [8] in order to analyze the vertical dynamic behaviour, when a bogie moves on a track in presence of three different types of practical imperfections: the corrugation of the rail head, the wheel flat and the case of a single sleeper that has lost its support due to erosion of the ballast. Hou et al. [9] reported their calculated responses for an asymmetrical vehicle/track model due to steady-state interaction and wheel flat.

The problem of the wheel/rail interaction may be solved by using two main types of models: a wheel rolling on the track and a moving irregularity between a stationary wheel and rail. The first model is the most realistic one, but it's also the most difficult to apply.

The track is actually a periodic infinite structure. The modal analysis requires truncating the track model after a finite number of spans. If the number of spans is large enough, the periodic structure of track may be obtained only at the central section of the model. When the wheel passes beyond this particular section, errors caused by the edge-approach effect occur. Thus, the length of the considered rail will be small, due to the boundary conditions. A practical solution for this issue is the cutting and merging method, proposed by Dong [10].

The model of a moving irregularity between a stationary wheel and rail is much easier to use especially for a continuously supported rail, when the error introduced is negligible. When it comes to the case of a sleeper-supported rail though, the whole system is subjected to parametric excitation due to the rail's dynamic stiffness variation. Wu and Thompson [11] have studied this issue and an equivalent time-varying model for the track in accordance with the space-varying receptance was used. They simulated the wheel/rail interaction caused by roughness excitation and the wheel flat/rail interaction using both the moving irregularity model and the moving wheel model. At the end, they have compared the results.

The wheel/rail interaction issue is a part of the area of dynamics of periodic structures under moving loads. Different aspects of the periodic structures under moving loads response have been studied by a number of researchers employing different methods. Floquet theorem was applied by Krzyzynski and Popp [12,13] in order to investigate the problem of vertical wave propagation in the track and its response under a moving harmonic force. Degrande et al. [14] have studied the vibrations in the free field from excitation due to metro trains in tunnels using the Floquet transform to reduce the discretization of the periodical structure of the tunnel to a single-bounded reference cell. In other paper, Clouteau et al. [15] have presented the importance of guided waves along the track using a substructure method based on Green's functions for the soil taken as a horizontally layered liner elastic half-space. Belotserkovskiy [16] has employed the so-called 'periodicity condition method' in order to determine the displacement of an Euler Bernoulli beam rested on an elastically periodic support under a moving harmonic force. Metrikine and Bosch [17] have evaluated the steady-state response of a two-level catenary to a uniformly moving pantograph using the periodicity condition method, as well. The steady-state vibration of a periodically supported beam on an elastic half-space under an uniformly moving harmonically varying load has been studied by Metrikine and Popp [18] using the equivalent stiffness of elastic half-space.

The present work deals with the issue of the wheel/rail interaction. The moving wheel on a discretely supported rail model was used. The vertical and longitudinal dynamics of the rail coupled to the rail pads were considered. At the rail pad, the rotation of the rail cross-sections is not free and the pinned–pinned resonance peaks are suppressed. For the vertical dynamics, the rail is treated as a uniform infinite Timoshenko beam. For longitudinal dynamics, the rail is taken as a uniform infinite bar. The sleepers are represented as rigid bodies with three d.o.f.'s—two longitudinal and vertical displacements and one rotation. This kind of model—a conventional Timoshenko beam model—may be used up to about 2000 Hz, as Wu and Thompson [19] showed.

The solution is based on applying the Green functions method. This method was also applied by Nordborg [20] but in a different manner. The Green functions applied to the track for the harmonic behaviour and for

time-domain analysis are determined. The two different types of Green functions are related through the Fourier transform. A Green matrix for the track was determined by considering the properties of the Green functions applied to the rail. This matrix solves the issue of simulating the wheel/rail interaction for any rail length. Using this matrix for the track model combined with a simple wheel model, three different aspects of the vertical wheel/rail vibration behaviour are investigated: the steady state of a wheel moving on the rail, the corrugated rail and the wheel flat.

2. The wheel/rail interaction model

In many applications of wheel/rail interaction, in which the natural frequencies of the vehicle suspension system are much lower than the ones of the wheel/rail vibration, it is good enough to model the vehicle simply as static load acting on the wheel including un-sprung mass.

A diagram of the wheel/track model is shown in Fig. 1. The wheel is regarded as an M_w mass which moves at a constant V speed along the rail. The vertical wheel displacement caused by the interaction with the rail is $z_w(t)$, where t stands for time. The initial position of the wheel is a.

The track model in which a rail is discretely supported by rail pads, semi-sleepers and ballast is considered. The rail is taken as a uniform infinite Timoshenko beam and as a bar with specific m mass per length unit. The bar theory is applied for longitudinal displacements of the rail. The other parameters for the rail are the Young's modulus E, the shear modulus G, the density ρ, the cross-sectional area S, the area moment of inertia I and the shear coefficient κ. The distance from the rail foot to the cross-section's neutral fibre is h. The loss factor of the rail is neglected. The vertical beam bend motion—$w(x, t)$ is the vertical displacement, $\theta(x, t)$ is the rotation of the cross-section—is coupled to the longitudinal motion—$u(x, t)$ is the longitudinal displacement—due to the rail pad.

The rail pad is modelled as a parallel connection of spring and dashpots having linear characteristics in x and z dimensions, and a similar torsion spring and damper restraining rotation in vertical–longitudinal plane. The elastic constants k_{rx}, k_{rz} and $k_{r\alpha}$ and the damping constants c_{rx}, c_{rz} and $c_{r\alpha}$ are related to the rail pad.

The ballast is represented by a system of parallel connections of springs and dashpots having viscose damping in x and z dimensions. The stiffnesses k_{bx}, k_{bz} and the viscous damping constants c_{bx}, c_{bz} refer to the ballast.

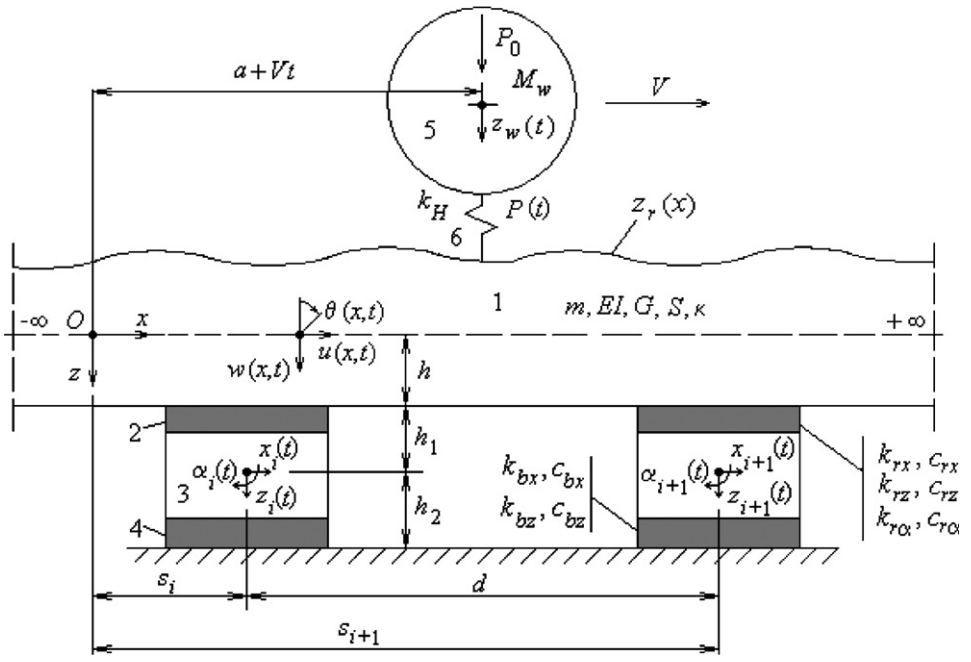

Fig. 1. Mechanical model of railway wheel on track: (1) rail; (2) rail-pad; (3) semi-sleeper; (4) ballast; (5) wheel; and (6) contact stiffness.

The semi-sleeper is considered as rigid body with three d.o.f.'s: the vertical translation $z_i(t)$, the lateral translation $x_i(t)$ (along the rail) and the rotation $\alpha_i(t)$ (across the rail). A semi-sleeper has the mass M_s and mass–moment of inertia I_s. The place of the sleeper i is s_i. The distances between the sleeper and the two elastic layers (modelling the rail pad and the ballast) are h_1 and h_2.

The equation describing the motion of the wheel is

$$M_w\ddot{z}_w(t) = P_0 - P(t), \tag{1}$$

where P_0 stands for the static wheel load and $P(t)$ the wheel/rail contact force.

The track's differential equations of motion can be written in matrix form as

$$\mathbf{L}_{x,t}\{\mathbf{q}\} + \sum_{i\in Z}(\mathbf{A}_t\{\mathbf{q}_i\} + \mathbf{B}_t\{\mathbf{q}_i^s\})\delta(x - s_i) = \{\mathbf{p}\}, \tag{2}$$

$$\mathbf{C}_t\{\mathbf{q}_i^s\} = \mathbf{D}_t\{\mathbf{q}_i\}, \tag{3}$$

where $\mathbf{L}_{x,t}$, $\mathbf{A}_t$, $\mathbf{B}_t$, $\mathbf{C}_t$ and $\mathbf{D}_t$ stand for matrix differentials (see Appendix A), $\{\mathbf{q}\} = \{\mathbf{q}(x,t)\} = [u(x,t)\ w(x,t)\ \theta(x,t)]^{\mathrm{T}}$ is the column vector of rail displacements, $\{\mathbf{q}_i\} = \{\mathbf{q}(s_i,t)\}$, $\{\mathbf{q}^s{}_i\} = \{\mathbf{q}^s{}_i(t)\} = [x_i(t)\ z_i(t)\ \alpha_i(t)]^{\mathrm{T}}$ is the column vector of the considered i sleeper's displacements, $\{\mathbf{p}\} = -P(t)\delta(x-a-Vt)\{\mathbf{e}\}$ is the column vector of forces on the rail with $\{\mathbf{e}\} = [0\,1\,0]^{\mathrm{T}}$ and $\delta(.)$ is the Dirac's delta function.

The wheel and the rail are solid elastic bodies and the deformation at the contact point can be expressed by Hertz's theory of elastic contact. According to this theory, the relationship between the contact force $P(t)$ and the Hertzian deflection:

$$z_\delta(t) = z_w(t) - w(a + Vt, t) - z_r(a + Vt)$$

is

$$[P(t)/C_H]^{2/3} = z_\delta(t)H[z_\delta(t)], \tag{4}$$

where $z_r(a+Vt)$ is the vertical excitation's displacement, due to roughness at the contact point, and C_H represents the Hertzian constant and $H[.]$ is the Heaviside function.

The boundary conditions are:

$$\lim_{|x-Vt|\to\infty}\{\mathbf{q}(x,t)\} = [0\quad 0\quad 0]^{\mathrm{T}}, \quad \lim_{i\to\pm\infty}\{\mathbf{q}_i^s(t)\} = [0\quad 0\quad 0]^{\mathrm{T}} \tag{5}$$

and the initial conditions are:

$$\begin{aligned} &z_w(0) = 0, \quad \dot{z}_w(0) = 0, \quad \{\mathbf{q}(x,0)\} = [0\quad 0\quad 0]^{\mathrm{T}}, \quad \{\dot{\mathbf{q}}(x,0)\} = [0\quad 0\quad 0]^{\mathrm{T}},\\ &\{\mathbf{q}_i^s(0)\} = [0\quad 0\quad 0]^{\mathrm{T}}, \quad \{\dot{\mathbf{q}}_i^s(0)\} = [0\quad 0\quad 0]^{\mathrm{T}}. \end{aligned} \tag{6}$$

By the use of the track's Green functions, the model's equations may be solved and the wheel–track interaction may be simulated.

3. The track's Green functions

Generally speaking, the issue of track vibration may be solved using the Green functions method, for both the frequency-domain and time-domain analysis. The objective of this section is to define and describe the track's Green functions.

3.1. Defining and calculating the track's Green functions

The Green functions for frequency-domain analysis have complex values and depend on the angular frequency marked here as ω. These will be named as 'the Green complex functions'. The Green functions for time-domain analysis are time dependent and have real values—these will be named as 'real Green functions'. The complex Green functions are the Fourier transforms of the real Green functions.

The time-domain analysis of the track's dynamic response for a vertical excitation may be studied using two real types of Green functions. One of those is the column vector of rail's real Green functions (including the

rail's response in the x section at the $t-\tau$ moment, if at the τ moment in the ξ section an impulse force occurred):

$$\{\mathbf{g}(x,\xi,t-\tau)\} = [\, g_u(x,\xi,t-\tau) \quad g_w(x,\xi,t-\tau) \quad g_\theta(x,\xi,t-\tau)\,]^{\mathrm{T}}. \tag{7}$$

The other type of Green functions is the Green functions' vector:

$$\{\mathbf{g}_i^s(\xi,t-\tau)\} = [\, g_{ix}(\xi,t-\tau) \quad g_{iz}(\xi,t-\tau) \quad g_{i\alpha}(\xi,t-\tau)\,]^{\mathrm{T}}, \tag{8}$$

which contains the 'i' sleeper response at $t-\tau$ moment, if at the τ moment in section ξ an impulse force occurred.

The Green's functions are the solutions for Eqs. (2) and (3) if the right term of the first equation is

$$\{\mathbf{p}\} = \delta(x-\xi)\delta(t-\tau)\{\mathbf{e}\}. \tag{9}$$

The track's complex Green functions are two different types: the column vector of rail's complex Green functions consisting in the rail's response in the x section, caused by a unitary harmonic impulse force by an angular ω frequency, occurring in the ξ section:

$$\{\mathbf{G}(x,\xi,\omega)\} = [\, G_u(x,\xi,\omega) \quad G_w(x,\xi,\omega) \quad G_\theta(x,\xi,\omega)\,]^{\mathrm{T}} = F[\{\mathbf{g}(x,\xi,t)\}] \tag{10}$$

and the column vector of the sleeper's complex Green functions consisting in the 'i' sleeper's response, caused by the same unitary harmonic impulse force:

$$\{\mathbf{G}_i^s(\xi,\omega)\} = [\, G_{ix}(\xi,\omega) \quad G_{iz}(\xi,\omega) \quad G_{i\alpha}(\xi,\omega)\,]^{\mathrm{T}} = F[\{g_i^s(\xi,t)\}], \tag{11}$$

where $F\,[.]$ is the Fourier transform. All complex Green functions are receptances.

Using the reverse Fourier transform and the complex track's Green functions, the real Green functions for the track may be calculated:

$$\begin{aligned}\{\mathbf{g}(x,\xi,t-\tau)\} &= \frac{1}{2\pi}\int_{-\infty}^{\infty}\{\mathbf{G}(x,\xi,\omega)\}\exp[\mathrm{j}\omega(t-\tau)]\,\mathrm{d}\omega \\ &= \frac{2}{\pi}\int_{0}^{\infty}\mathrm{Re}\{\mathbf{G}(x,\xi,\omega)\}\cos[\omega(t-\tau)]\,\mathrm{d}\omega,\end{aligned} \tag{12}$$

$$\begin{aligned}\{\mathbf{g}_i^s(\xi,t-\tau)\} &= \frac{1}{2\pi}\int_{-\infty}^{\infty}\{\mathbf{G}_i^s(\xi,\omega)\}\ \exp[\mathrm{j}\omega(t-\tau)]\,\mathrm{d}\omega \\ &= \frac{2}{\pi}\int_{0}^{\infty}\mathrm{Re}\{\mathbf{G}_i^s(\xi,\omega)\}\ \cos[\omega(t-\tau)]\,\mathrm{d}\omega,\end{aligned} \tag{13}$$

where $\mathrm{j}^2 = -1$. Eqs. (12) and (13) are valid because all real Green functions are causal.

It's obvious that the complex Green functions are in fact the solutions of the following equations:

$$\mathbf{L}_{x,\omega}\{\mathbf{G}\} + \sum_{i\in Z}(\mathbf{A}_\omega\{\mathbf{G}_i\} + \mathbf{B}_\omega\{\mathbf{G}_i^s\})\delta(x-s_i) = \delta(x-\xi)\{\mathbf{e}\}, \tag{14}$$

$$\mathbf{C}_\omega\{\mathbf{G}_i^s\} = \mathbf{D}_\omega\{\mathbf{G}_i\}, \tag{15}$$

where by simplicity purposes, the following were marked as $\{\mathbf{G}\} = \{\mathbf{G}(x,\xi,\omega)\}$, $\{\mathbf{G}_i\} = \{\mathbf{G}(s_i,\xi,\omega)\}$, $\{\mathbf{G}^s{}_i\} = \{\mathbf{G}^s{}_i(\xi,\omega)\}$ and $\mathbf{L}_{x,\omega} = F[\mathbf{L}_{x,t}]$, $\mathbf{A}_\omega = F[\mathbf{A}_t]$, etc.

By extracting $\{\mathbf{G}^s{}_i\}$ from Eq. (15) and substituting it in Eq. (14) the following results:

$$\mathbf{L}_{x,\omega}\{\mathbf{G}\} = \delta(x-\xi)\{\mathbf{e}\} - \sum_{i\in Z}\mathbf{K}_\omega\{\mathbf{G}_i\}\delta(x-s_i), \tag{16}$$

with $\mathbf{K}_\omega = \mathbf{A}_\omega + \mathbf{B}_\omega\mathbf{C}_\omega^{-1}\mathbf{D}_\omega$.

Eq. (16) is then multiplied by the matrix operator:

$$\mathbf{J}_x = \begin{bmatrix} 1 & 0 & 0 \\ 0 & \dfrac{EI}{GS\kappa}\dfrac{\mathrm{d}^2}{\mathrm{d}x^2} + \dfrac{\rho I\omega^2}{GS\kappa} - 1 & \dfrac{\mathrm{d}}{\mathrm{d}x} \\ 0 & -\dfrac{\mathrm{d}}{\mathrm{d}x} & \dfrac{\mathrm{d}^2}{\mathrm{d}x^2} + \dfrac{\omega^2 m}{GS\kappa} \end{bmatrix} \tag{17}$$

and the $\mathbf{L}_{x,\omega}$ operator becomes diagonal. The solutions of Eq. (16) may be written as follows:

$$\{\mathbf{G}\} = \int_{-\infty}^{\infty} \mathbf{\Gamma}\left[\mathbf{J}_{x'}\delta(x'-\xi)\{\mathbf{e}\} - \sum_{i\in Z}\mathbf{J}_{x'}\delta(x'-s_i)\mathbf{K}_\omega\{\mathbf{G}_i\}\right]\mathrm{d}x', \tag{18}$$

where $\mathbf{\Gamma}$ stands for the diagonal operator's Green's functions matrix:

$$\mathbf{L}^*_{x,\omega} = \mathbf{J}_x\mathbf{L}_{x,\omega} = \mathrm{diag}(H_{1x}, H_{2x}, H_{2x}) = \begin{bmatrix} H_{1x} & 0 & 0 \\ 0 & H_{2x} & 0 \\ 0 & 0 & H_{2x} \end{bmatrix}, \tag{19}$$

with

$$H_{1x} = ES\frac{\mathrm{d}^2}{\mathrm{d}x^2} + m\omega^2, \quad H_{2x} = EI\frac{\mathrm{d}^4}{\mathrm{d}x^4} + \omega^2\left(m\frac{EI}{\kappa SG} + \rho I\right)\frac{\mathrm{d}^2}{\mathrm{d}x^2} + m\omega^2\left(\frac{\rho\omega^2 I}{\kappa SG} - 1\right).$$

The $\mathbf{\Gamma}$ matrix of Green's functions is the solution of the following equation:

$$\mathbf{L}^*_{x,\omega}\mathbf{\Gamma} = \delta(x-x')\mathbf{E}, \tag{20}$$

where $\mathbf{E}$ stands for the 3×3 unity matrix.

The $\mathbf{\Gamma}$ matrix has the following shape:

$$\mathbf{\Gamma} = \mathbf{\Gamma}(x,x',\omega) = \mathrm{diag}(\Gamma^u(x,x',\omega), \Gamma^w(x,x',\omega), \Gamma^\theta(x,x',\omega)), \tag{21}$$

in which

$$\Gamma^u(x,x',\omega) = \mathrm{j}\frac{\exp(-\mathrm{j}\beta|x-x'|)}{2\beta SE},$$

is the Green's functions of an infinite bar, and

$$\Gamma^w(x,x',\omega) = \Gamma^\theta(x,x',\omega) = -\frac{\beta_2\,\exp(-\beta_1|x-x'|) + \mathrm{j}\beta_1\,\exp(-\mathrm{j}\beta_2|x-x'|)}{2\beta_1\beta_2(\beta_1^2+\beta_2^2)EI}$$

are the Green's functions of an infinite Timoshenko beam [21], where

$$\beta = \sqrt{\frac{m\omega^2}{SE}}, \quad \beta_{1,2} = \sqrt{\sqrt{\frac{\rho^2\omega^4}{4E^2}\left(\frac{E}{G\kappa}-1\right)^2 + \frac{m\omega^2}{EI}} \mp \frac{\rho\omega^2}{2E}\left(\frac{E}{G\kappa}+1\right)}$$

and $\omega^2 \leqslant GS\kappa/(\rho I)$.

Taking

$$\mathbf{\Gamma}^*(x,\xi,\omega) = \int_{-\infty}^{\infty}\mathbf{\Gamma}(x,x',\omega)\mathbf{J}_{x'}\delta(x'-\xi)\,\mathrm{d}x',$$

respectively

$$\mathbf{\Gamma}^*(x,\xi,\omega) = \mathrm{diag}\left(\Gamma^u(x,\xi,\omega), \frac{EI}{GS\kappa}\Gamma^w_{x'x'}(x,\xi,\omega) + \left(\frac{\rho I\omega^2}{GS\kappa} - 1\right)\right.$$
$$\left.\Gamma^w(x,\xi,\omega), \Gamma^\theta_{x'x'}(x,\xi,\omega) + \frac{\omega^2 m}{GS\kappa}\Gamma^\theta(x,\xi,\omega)\right).$$

Eq. (18) can be written as

$$\{\mathbf{G}\} = \mathbf{\Gamma}^*(x, \xi, \omega)\{\mathbf{e}\} - \sum_{i \in Z} \mathbf{\Gamma}^*(x, s_i, \omega)\mathbf{K}_\omega\{\mathbf{G}_i\}. \tag{22}$$

The calculation for rail displacements near the 'k' sleeper is going to be done by the use of Eq. (22) in which $\{\mathbf{G}\}$ will be replaced by $\{\mathbf{G}_k\}$. Thus, the following will result:

$$\{\mathbf{G}(s_k, \xi, \omega)\} = \{\mathbf{P}_k\} - \sum_{i \in Z} \mathbf{\Gamma}^*(s_k, s_i, \omega)\mathbf{K}_\omega\{\mathbf{G}(s_i, \xi, \omega)\}, \tag{23}$$

where $\{\mathbf{P}_k\} = \mathbf{\Gamma}^*(s_k, \xi, \omega)\{\mathbf{e}\}$.

Finally, by considering a number of n sleepers (with n sufficiently as large), the following matrix equation results:

$$\begin{bmatrix} \mathbf{\Gamma}^*_{1,1}\mathbf{K}_\omega + \mathbf{E} & \mathbf{\Gamma}^*_{1,2}\mathbf{K}_\omega & \cdots & \mathbf{\Gamma}^*_{1,n}\mathbf{K}_\omega \\ \mathbf{\Gamma}^*_{2,1}\mathbf{K}_\omega & \mathbf{\Gamma}^*_{2,2}\mathbf{K}_\omega + \mathbf{E} & \cdots & \mathbf{\Gamma}^*_{2,n}\mathbf{K}_\omega \\ \cdots & \cdots & \cdots & \cdots \\ \mathbf{\Gamma}^*_{n,1}\mathbf{K}_\omega & \mathbf{\Gamma}^*_{n,2}\mathbf{K}_\omega & \cdots & \mathbf{\Gamma}^*_{n,n}\mathbf{K}_\omega + \mathbf{E} \end{bmatrix} \begin{bmatrix} \{\mathbf{G}_1\} \\ \{\mathbf{G}_2\} \\ \cdots \\ \{\mathbf{G}_n\} \end{bmatrix} = \begin{bmatrix} \{\mathbf{P}_1\} \\ \{\mathbf{P}_2\} \\ \cdots \\ \{\mathbf{P}_n\} \end{bmatrix}, \tag{24}$$

with $\mathbf{\Gamma}^*_{k,i} = \mathbf{\Gamma}^*(s_k, s_i, \omega)$ and $k,\ i = 1 \div n$. The equation's matrix depends on the sleeper positions and the angular frequency.

The rail's Green functions are particularly important because they are used to determine the wheel/rail contact forces. The track is considered as an infinite periodic and damped mechanical structure. The rail's Green functions have three outstanding properties:

- They are symmetrical (the Maxwell–Betty principle):

$$G_w(x, \xi, \omega) = G_w(\xi, x, \omega), \quad g_w(x, \xi, t-\tau) = g_w(\xi, x, t-\tau). \tag{25}$$

- They are attenuated in space, time and frequency-domains:

$$\lim_{x \to \pm\infty}\{\mathbf{G}(x, \xi, \omega)\} = \lim_{\xi \to \pm\infty}\{\mathbf{G}(x, \xi, \omega)\} = \lim_{\omega \to \pm\infty}\{\mathbf{G}(x, \xi, \omega)\} = 0, \tag{26a}$$

$$\lim_{x \to \pm\infty}\{\mathbf{g}(x, \xi, t-\tau)\} = \lim_{\xi \to \pm\infty}\{\mathbf{g}(x, \xi, t-\tau)\} = \lim_{t-\tau \to +\infty}\{\mathbf{g}(x, \xi, t-\tau)\} = 0. \tag{26b}$$

- They are periodical:

$$\begin{aligned} \{\mathbf{G}(x, \xi, \omega)\} &= \{\mathbf{G}(x + kd, \xi + kd, \omega)\}, \\ \{\mathbf{g}(x, \xi, t-\tau)\} &= \{\mathbf{g}(x + kd, \xi + kd, t-\tau)\}, \end{aligned} \tag{27}$$

  where k is an integer.

The sleepers' Green functions are attenuated in space, time and frequency-domains:

$$\lim_{i \to \pm\infty}\{\mathbf{G}^s_i(\xi, \omega)\} = \lim_{\xi \to \pm\infty}\{\mathbf{G}^s_i(\xi, \omega)\} = \lim_{\omega \to \pm\infty}\{\mathbf{G}^s_i(\xi, \omega)\} = 0, \tag{28a}$$

$$\lim_{i \to \pm\infty}\{\mathbf{g}^s_i(\xi, t-\tau)\} = \lim_{\xi \to \pm\infty}\{\mathbf{g}^s_i(\xi, t-\tau)\} = \lim_{t-\tau \to +\infty}\{\mathbf{g}^s_i(\xi, t-\tau)\} = 0 \tag{28b}$$

and they are periodical:

$$\{\mathbf{G}^s_i(\xi, \omega)\} = \{\mathbf{G}^s_{i+k}(\xi + kd, \omega)\}, \quad \{\mathbf{g}^s_i(\xi, t-\tau)\} = \{\mathbf{g}^s_{i+k}(\xi + kd, t-\tau)\}. \tag{29}$$

The rail's vertical displacement at the contact point has an appropriate real $g_w(a+Vt,\ a+V\tau,\ t-\tau)$ Green function that has to be used when the wheel or the vertical force is moving at a certain V speed. This function

results actually from the real $g_w(x,\xi,t-\tau)$ Green function and keeps its original properties. Basically, the $g_w(a+Vt,a+V\tau,t-\tau)$ function can generate a matrix and the wheel's rolling on the rail may be simulated at any moment and for any distance.

3.2. Numerical application and discussions

The complex and real rail's Green functions are calculated for the particular case of a discretely supported UIC 60 rail. The parameters for the rail are: $E=210\,\text{GPa}$, $G=8.08\,\text{GPa}$, $\kappa=0.4$, $\rho=7850\,\text{kg/m}^3$, $S=7.69\times10^{-3}\,\text{m}^2$ and $I=30.55\times10^{-6}\,\text{m}^4$.

The parameters for the discrete support are chosen as follows: $M_s=160\,\text{kg}$, $I_s=1.586\,\text{kg m}^2$, $d=0.6\,\text{m}$, $h=0.08\,\text{m}$, $h_1=0.116\,\text{m}$, $h_2=0.114\,\text{m}$, $k_{rx}=50\,\text{MN/m}$, $k_{rz}=350\ \text{MN/m}$, $k_{r\alpha}=k_{rz}c^2/3=746.7\,\text{kN m/rad}$ ($2c=160\,\text{mm}$, rail pad width), $c_{rx}=10\,\text{kN s/m}$, $c_{rz}=48\,\text{kN s/m}$, $c_{r\alpha}=c_{rz}c^2/3=102.4\,\text{N ms/rad}$, $k_{bx}=39.6$ MN/m, $k_{bz}=70\,\text{MN/m}$, $c_{bx}=52\,\text{kN s/m}$, and $c_{bz}=47\,\text{kN s/m}$.

The present rail pad and ballast stiffness are chosen by considering data from two previous studies [22,23]. The damping is chosen to give a good fit to the test results [22]. The model of the rail's structural damping is studied in the works mentioned above. This model may be used though, only in the frequency-domain analysis and not at all in the time-domain analysis. For this reason, the viscosity damper model is considered in the present study.

For the numerical simulation, the track model length is 40 sleeper bays. The origin of the referential system is placed at sleeper no. 21.

The complex Green function of the vertical displacement of the rail at the point of a unitary harmonic excitation both for excitation acting at mid span and for excitation acting above a sleeper is shown in Fig. 2 in the domain of 10 Hz–5 kHz. The complex Green function for the sleeper under a vertical excitation from above is also presented. The response of the rail at low frequencies is dominated by two peaks at about 95 and 550 Hz because the rail and the sleepers are a vibration system with two elastic layers. An anti-resonance frequency appears at approximately 260 Hz. It is actually the vibration absorber effect due to the sleepers. At frequencies below the anti-resonance frequency there are no significant differences between excitations above the sleeper and at mid span. At higher frequencies though, the vertical rail displacement at mid span is higher.

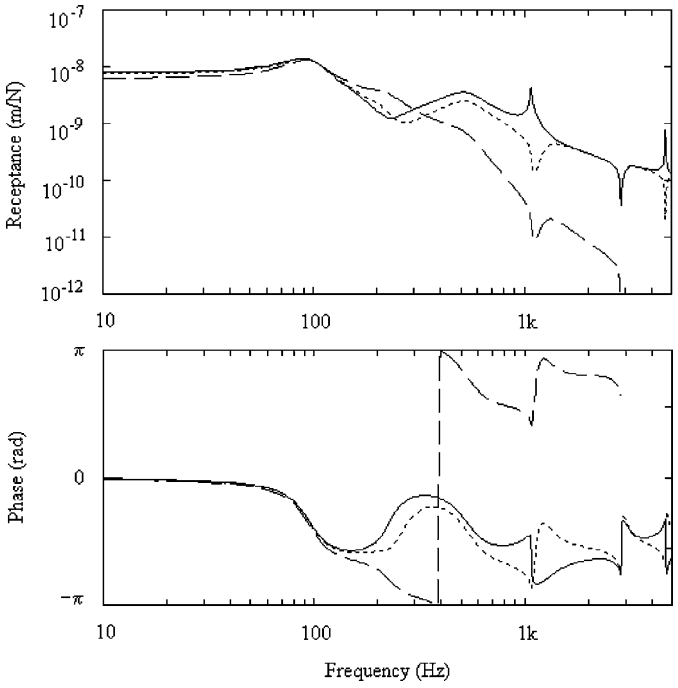

Fig. 2. Complex Green functions of the track: ———, the rail at mid span; · · · · ·, the rail above sleeper; and – – –, the sleeper.

The first pinned–pinned resonance appears around 1075 Hz. At this frequency, the vertical bending wavelength equals twice the span. The anti-resonance frequency may be observed at about 1120 Hz for above sleeper excitation. It is the 'elastic sleeper support' effect.

The second pinned–pinned resonance frequency is around 2875 Hz. At this frequency, the vertical bending wavelength equals the span. The receptance is minimal for both excitations, at mid span and above the sleeper. When the vertical bending wavelength equals 2/3 of a span, a third pinned–pinned frequency occurs. Its value is around 4670 Hz. The receptance its maximum when excitation is placed at mid span and its minimal when excitation is placed right above the sleeper.

The sleeper's receptance is smaller than the rail's, especially when dealing with high frequencies. Around the anti-resonance frequency of 260 Hz, the sleeper behaves as a dynamic absorber for the rail and its receptance is higher than the rail's.

The vertical accelerances of the rail are shown in Fig. 3. By comparing these diagrams with those in Ref. [22], which show the same trends for the experimental results, it can be seen that the present model might be used successfully for vertical rail vibrations up to about 2000 Hz. At higher frequencies though, the rail does not behave like a beam anymore, its foot vibrating much more intense than its head. Anyway, the model might be used in predicting the vibration of the rail's head at frequencies up to 5 kHz.

The track foundation damping has very little effect on the response of the rail at pinned–pinned resonance frequency. On the other hand, this is limited because the sleepers are not equidistant and the contact between the rail and pads is distributed. However, in the theoretical models, the sleeper bay is assumed to be constant and the rail pad is taken as discrete support. Thus, the predictable results are in discrepancy with the theoretic ones. In order to correct the theoretical results, one can add extra damping to the rail [19].

In this particular work, although the sleepers are equidistant, the structural damping is neglected and the rail is assumed as ideally point-supported, the rail's response to the pinned–pinned resonance frequency matches the experimental result. That's because the rail's cross-section limited rotation due to the rail pad is considered.

The pinned–pinned resonance frequency value is little influenced because the rail pad presents an elastic withstanding along the rail and to rotation, as shown in Fig. 4. The shape of pinned–pinned resonance peak is not that sharp, because the rail pad has damping displacements along the rails and rotations. This particular aspect is shown in Fig. 5.

As the track is a periodic structure, the appropriate complex Green function $G_w(x, \xi, \omega)$, will be periodic as well. For the numerical simulation, the track's length is finite. Thus, the complex Green function is not rigorously periodic. Fig. 6 presents the periodic relative error:

$$\varepsilon = \frac{\left|G_w(x + kd, \xi + kd, \omega)\right| - \left|G_w(x, \xi, \omega)\right|}{\left|G_w(x, \xi, \omega)\right|},$$

for a number of $k = 4$ span lengths ($x = \xi = 0.3$) and for $k = 5$ ($x = \xi = 0$). Some low percentage errors occur around the pinned–pinned resonance frequencies.

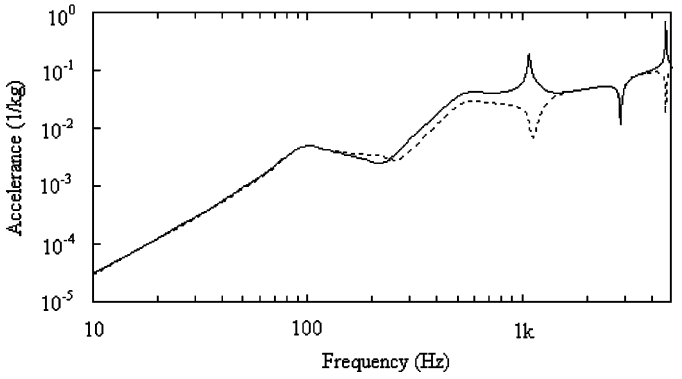

Fig. 3. Rail accelerances: ———, at mid span; and · · · · ·, above sleeper.

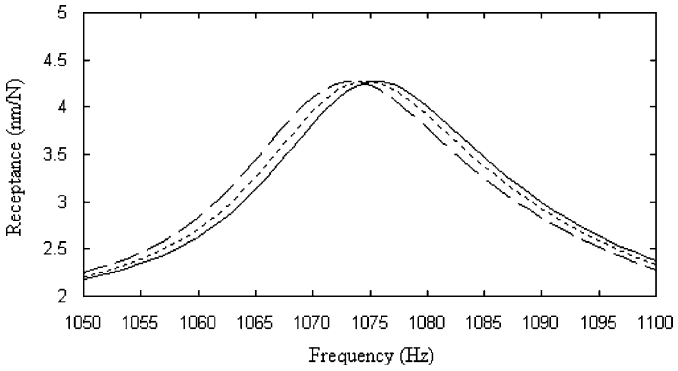

Fig. 4. Rail receptance at pinned–pinned resonance for different rail pad stiffness: ———, $k_{rx} = 50$ MN/m, $k_{r\alpha} = 746.7$ kN m/rad; · · · · ·, $k_{rx} = 25$ MN/m, $k_{r\alpha} = 746.7$ kN m/rad; – – –, $k_{rx} = 50$ MN/m, $k_{r\alpha} = 373.3$ kN m/rad.

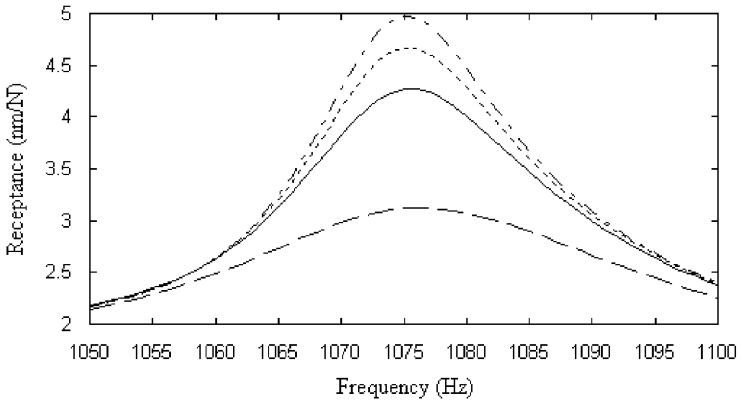

Fig. 5. Rail receptance at pinned–pinned resonance for different rail pad damping: ———, $c_{rx} = 10$ kN s/m, $c_{r\alpha} = 102.4$ Nm s/rad; · · · · ·, $c_{rx} = 5$ kN s/m, $c_{r\alpha} = 102.4$ Nm s/rad; – · – · –, $c_{rx} = 10$ kN s/m, $c_{r\alpha} = 51.2$ Nm s/rad; – – –, $c_{rx} = 20$ kN s/m, $c_{r\alpha} = 204.8$ Nm s/rad.

The propagation of the bending waves along the track is damped and selective. Fig. 7 presents the attenuation ratio as

$$A = \left| \frac{G_w(x, x + kd, \omega)}{G_w(x, x, \omega)} \right|,$$

at $k = 3$, 5, 7 span lengths when excited at mid span. The bending wave for pinned–pinned resonance frequencies has the best propagation. This aspect may be observed in Fig. 8, which presents the decay rates of vertical vibration along the rail for the first three resonance frequencies (95, 550 and 1075 Hz) and the force acting at mid span. The decay rate is about 6.5 dB/m at 95 Hz, 8.7 dB/m at 550 Hz and 1.3 dB/m at 1075 Hz. This decay rate was calculated from the attenuation in vibration level over a 9 span length from the excitation point divided by this distance. The predicted results match the experimental ones [22].

The complex Green functions are used to calculate the track's real Green functions. Eqs. (12) and (13) are numerically integrated using the help of the cubic spline functions. The integration domain was chosen between 0 and 2872 Hz, which was the second pinned–pinned resonance frequency. The receptance at this frequency is very small, 0.036 nm/N. The integration step was chosen as 8 Hz. This value is a compromise between the calculus precision and its efficiency. Fig. 9 presents the rail's real Green function for mid span-applied impulse ($x = 0.3$, $\xi = 0.3$). The maximal value of this Green function is 6.52 μm/(N s). After approximately 7 ms, the Green function is dominated by two mixed oscillations. The first one has a frequency of 95 Hz and the other one's frequency is 1075 Hz. One can see that the Green function is damped. After another 80 ms, its amplitude decreases below 2 nm/(N s), which is less than 1/325 from its maximum value. Practically, the Green function fades away completely after 80–100 ms.

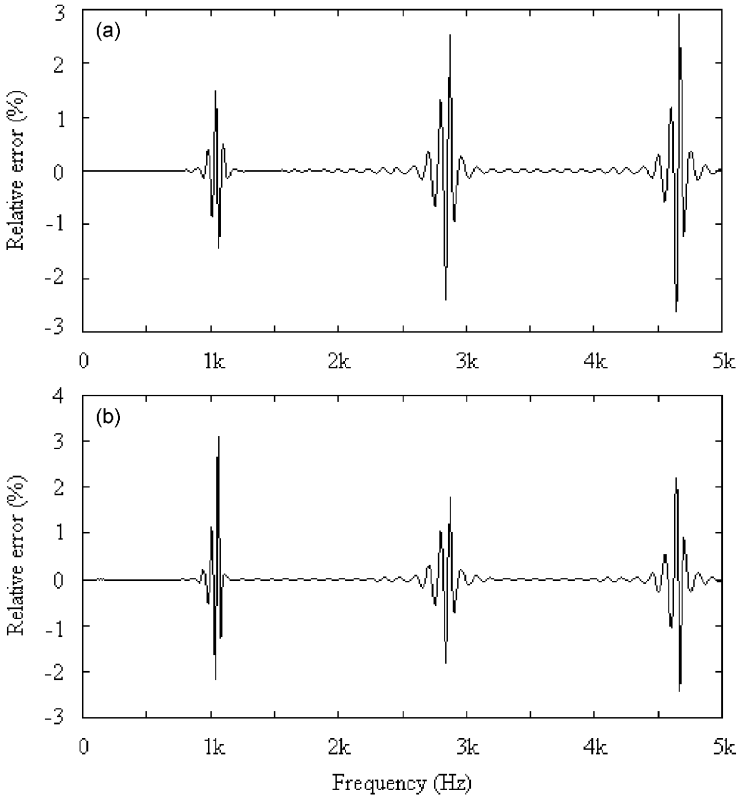

Fig. 6. The rail receptance periodic error: (a) at mid span for $k = 4$; and (b) above the sleeper for $k = 5$.

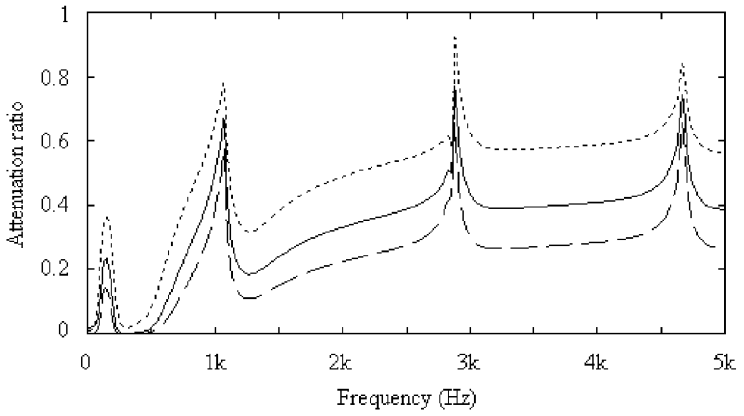

Fig. 7. Attenuation ratio of the rail receptance: · · · · ·, for 3 sleeper bays; ———, for 5 sleeper bays; and – – – for 7 sleeper bays.

Fig. 10 presents the rail's real Green function for sleeper applied impulse ($x = 0$, $\xi = 0$). In this particular case, the rail is less sensitive, and the maximum value is 4.035 μm/(N s). The function is strongly damped and literally dominated by a 95 Hz component.

Fig. 11 shows the rail response at mid span when the impulse is applied 7 sleepers away ($x = 2.1$, $\xi = -2.1$). Because of the distance between the points of impulse appliance and response calculus, the response is delayed and its magnitude decreases. The maximum value for Green's function is 0.456 μm/(N s). The response is also damped and dominated by two different components of 95 and 1075 Hz, respectively.

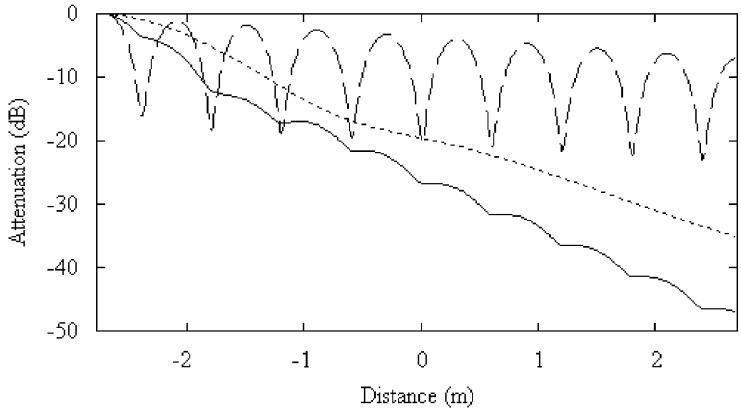

Fig. 8. Receptance attenuation along the rail: · · · · ·, for 95 Hz; ———, for 550 Hz; and – – –, for 1075 Hz.

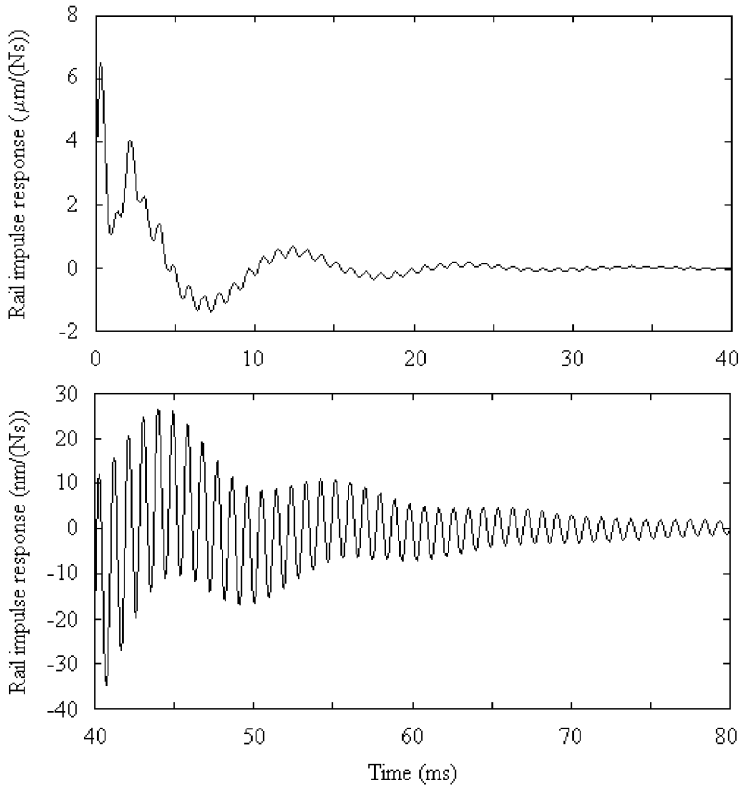

Fig. 9. The rail's real Green function at mid span ($x = 0{,}3$, $\xi = 0{,}3$).

Fig. 12 shows the rail's response above the sleeper, when the force impulse is applied 7 span lengths away ($x = 2.4$, $\xi = -1.8$). The response continues to be delayed and has a significantly smaller magnitude compared to the initial situation, when the impulse is applied right in the calculus point. The maximum value of the Green function is 0.298 μm/(N s).

And finally, the sleeper's Green function when applying the impulse above the sleeper is shown in Fig. 13. The sleeper's response is strongly damped and dominated by the 95 Hz component. The maximum value for the Green function is 3.606 μm/(N s).

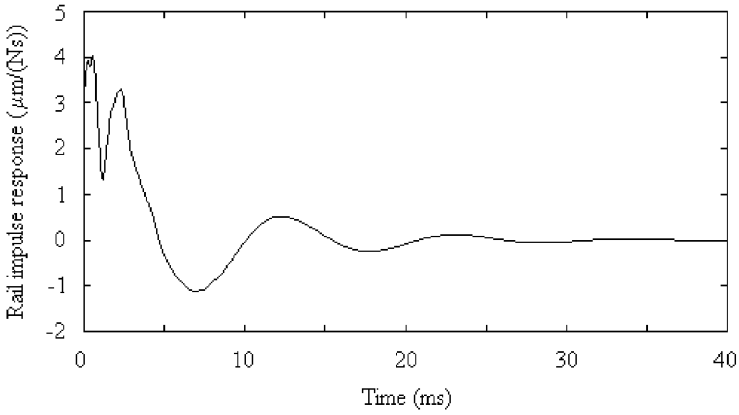

Fig. 10. The rail's real Green function above the sleeper ($x = 0$, $\xi = 0$).

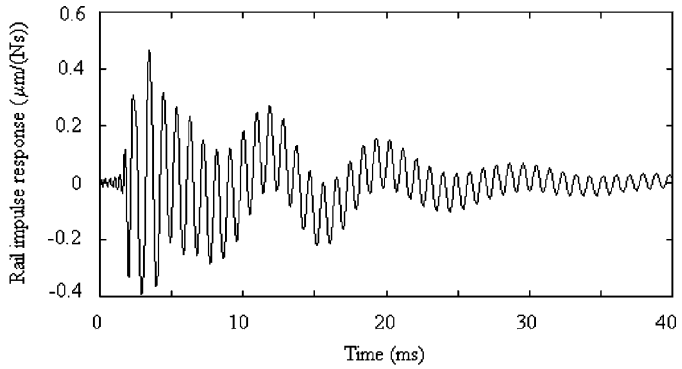

Fig. 11. The rail response at mid span when the impulse force is applied 7 sleeper bays away.

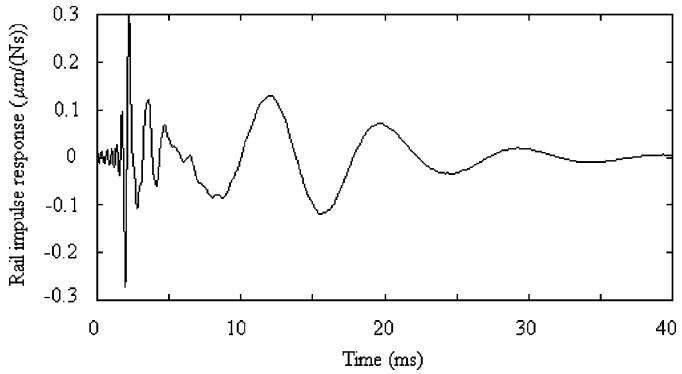

Fig. 12. The rail response at sleeper when the impulse force is applied 7 sleeper bays away.

4. The solution of the interaction problem

The main wheel/rail interaction problem is defined by Eqs. (1)–(4). It may be solved through numerical step-by-step integration. For this particular purpose, the wheel's motion equation will be written as

$$\dot{z}_w(t) = \dot{z}_w(0) + \frac{1}{M_w}\int_0^t [P_0 - P(\tau)]\mathrm{d}\tau, \quad z_w(t) = z_w(0) + \int_0^t \dot{z}_w(\tau)\mathrm{d}\tau. \tag{30}$$

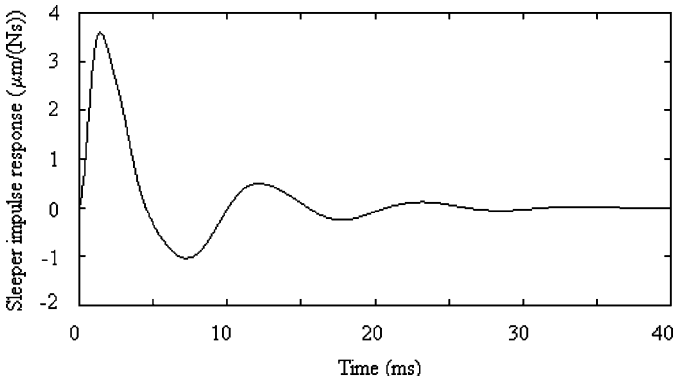

Fig. 13. The sleeper's real Green function for impact force applied above.

The rail displacement at the contact point may be determined using the Green function method:

$$w(a+Vt,t) = -\int_{-\infty}^{\infty}\int_{0}^{t} g_w(a+Vt,\xi,t-\tau)P(\tau)\delta(\xi-a-V\tau)\,\mathrm{d}\tau\,\mathrm{d}\xi$$
$$= -\int_{0}^{t} g_w(a+Vt,a+V\tau,t-\tau)P(\tau)\,\mathrm{d}\tau. \tag{31}$$

In other words, any $x=a+Vt$ contact point will have its appropriate Green function, $g_w(a+Vt, a+V\tau, t-\tau)$ depending on $\tau\in[0,t]$ only. A Green function has the particular property of being damped. Thus, as a result, there is a certain T for which the norm of Green function's $\|g_w\|$ is 'concentrated' in the $[0,T]$ interval:

$$\|g_w\| = \sqrt{(g_w,g_w)} = \left[\int_0^{\infty} g_w^2(a+Vt,a+V\tau,t-\tau)\,\mathrm{d}(t-\tau)\right]^{1/2}$$
$$\cong \left[\int_0^{T} g_w^2(a+Vt,a+V\tau,t-\tau)\,\mathrm{d}(t-\tau)\right]^{1/2}, \tag{32}$$

where $(.,.)$ is the inner product.

The Green function's contribution for $t-\tau>T$ can be even neglected:

$$g_w(a+Vt,a+V\tau,t-\tau)\cong 0, \quad \text{for } t\geqslant T. \tag{33}$$

From the practical point of view, it's quite enough to consider the $g_w(a+Vt, a+V\tau, t-\tau)$ sequence of Green function, where $t-\tau\in[0,T]$.

The Green function is also periodic:

$$g_w(a+V(t+kT_d),a+V(\tau+kT_d),t-\tau) = g_w(a+Vt,a+V\tau,t-\tau), \tag{34}$$

for $t-\tau\in[0,T]$, where $T_d=d/V$ and k is an integer. As a result, all the equidistant points situated at a span length, will share the same Green function.

When using the small time-steps method on short Δt time intervals in order to integrate the track's motion equations, there are a number of $N_g=T_d/\Delta t$ necessary Green functions to be calculated in $N_t=T/\Delta t+1$ points. All the Green functions are assembled in a rectangular $N_g\times N_t$ matrix. This matrix can be defined as the track's Green matrix.

It is interesting to notice that this matrix includes also the values necessary for the integration of the motion equations for the $0<t<T$—the transitory period of numeric integration. Next, the whole track's Green matrix is used to integrate the track's motion equations for any $t>T$. This particular period may be considered as the 'stationary' period of numeric integration.

For the numeric calculus, a certain $t_0,t_1,\ldots,t_n$ (with $t_0=0$, $t_n=t$ and $\Delta t=t_i-t_{i-1}$ where $i=1\div n$) time partition is considered. The equations for wheel and rail displacement may be written under the

recurrent form:

$$\dot{z}_w(t_n) = \dot{z}_w(t_{n-1}) + \frac{1}{M_w}\int_{t_{n-1}}^{t_n}[P_0 - P(\tau)]\mathrm{d}\tau, \tag{35}$$

$$z_w(t_n) = z_w(t_{n-1}) + \int_{t_{n-1}}^{t_n}\dot{z}_w(\tau)\mathrm{d}\tau, \tag{36}$$

$$w(a + Vt_n, t_n) = -\sum_{i=1}^{n}\int_{t_{i-1}}^{t_i} g_w(a + Vt_n, a + V\tau, t_n - \tau)P(\tau)\mathrm{d}\tau. \tag{37}$$

The integrations will be calculated adopting the hypothesis that in the $[t_{i-1}, t_i]$ time interval, the contact force $P(\tau)$ and the Green function will have a linear variation. As a result, the following will occur:

$$\dot{z}_w(t_n) = \dot{z}_w(t_{n-1}) + \frac{\Delta t}{M_w}\left[P_0 - \frac{P(t_n) + P(t_{n-1})}{2}\right], \tag{38}$$

$$z_w(t_n) = z_w(t_{n-1}) + \dot{z}_w(t_{n-1})\Delta t + \frac{\Delta t^2}{2M_w}\left[P_0 - \frac{P(t_n) + 2P(t_{n-1})}{3}\right], \tag{39}$$

$$w(a + Vt_n, t_n) = -\Delta t\sum_{j=1}^{n}\left\{\frac{g_w(t_{j-1})P(t_j) + g_w(t_j)P(t_{j-1})}{2} + \frac{[g_w(t_j) - g_w(t_{j-1})][P(t_j) - P(t_{j-1})]}{3}\right\}, \tag{40}$$

where $g_w(t_j) = g_w(a + Vt_n, a + Vt_j, t_n - t_j)$.

It is obvious that the wheel displacement and the rail deflection at the contact point are strongly influenced by the amplitude of the $P(t_n)$ contact force. By substituting Eqs. (39) and (40) into Eq. (4), a non-linear $P(t_n)$ based equation results. Solving this equation in an iterative manner, the $P(t_n)$ contact force is determined at each integration step. Then, the wheel displacement and the rail deflection are determined. After that, the procedure repeats with the next step.

5. Numerical application

For the numeric simulation, the same parameters for the rail together with a wheel were considered $M_w = 550\,\mathrm{kg}$, including the axle's un-sprung mass. The Hertzian constant $C_H = 11.86 \times 10^{10}\,\mathrm{N/m^{3/2}}$ is determined taking the curve radiuses of 0.3 m and ∞ for the rail, and 0.5 and 0.46 m for the wheel. This corresponds to a wheel having a 920 mm diameter and an S 78 rolling profile (used at CFR) on UIC 60 rail. The wheel static load is 100 kN.

5.1. The wheel/rail harmonic behaviour

Prior to presenting the numeric simulation results in the time-domain, it is useful to examine the harmonic behaviour of the wheel/rail system assuming the moving roughness model. The Hertzian contact is assumed to be linear having the k_H stiffness of 1.028 GN/m. The numerical simulations for the harmonic behaviour were made considering two particular situations: wheel above a sleeper and wheel at mid span.

The wheel/rail system's response is correlated with the receptances of the two bodies and contact elasticity (Fig. 14). At low frequencies (below 60 Hz), the wheel receptance is higher than the rail's. At frequencies above 60 Hz, the ratio reverses. In this frequency range, the contact elasticity is much smaller than the rail receptance. Due to the dynamic absorber effect given by the sleepers, close to the rail's anti-resonance frequency, the wheel and rail receptances are matching with the contact elasticity. Finally, in the pinned–pinned resonance/anti-resonance zone, the rail receptance is close to the contact elasticity.

Fig. 15 shows the rail and wheel displacements. The wheel/rail contact force is presented in Fig. 16, as well. All sizes are compared to roughness. The wheel/rail system has two resonances, one at low frequencies of about 60 Hz, and the other at medium frequencies of about 240 Hz. The wheel displacement is higher than

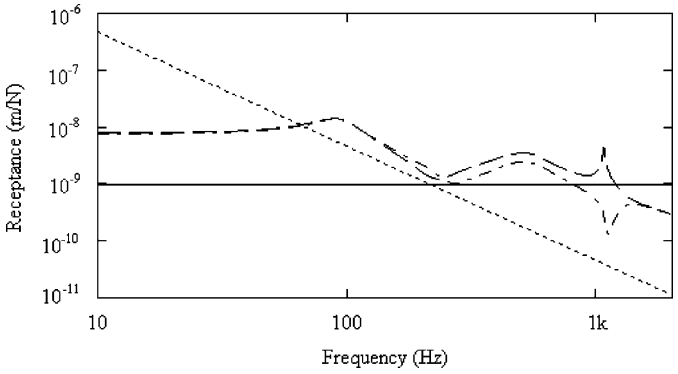

Fig. 14. The receptances of wheel/rail: – – –, rail between sleepers; – · – · –, rail above sleeper; · · · · ·, wheel; ———, elasticity of contact.

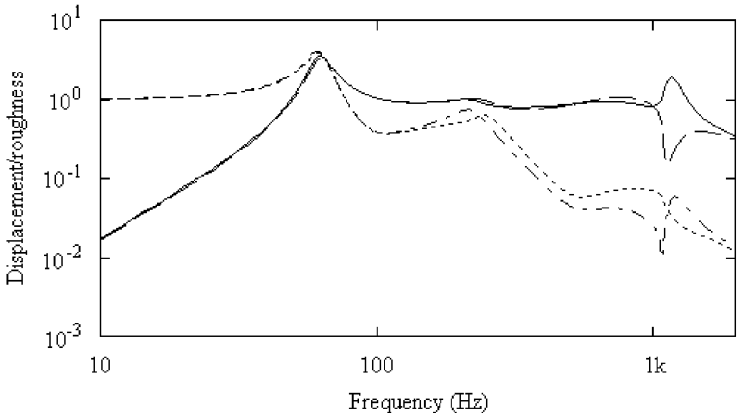

Fig. 15. Wheel/rail harmonic response: ———, rail between sleepers; – – –, rail above sleeper; – · – · –, wheel between sleeper; and · · · · ·, wheel above sleeper.

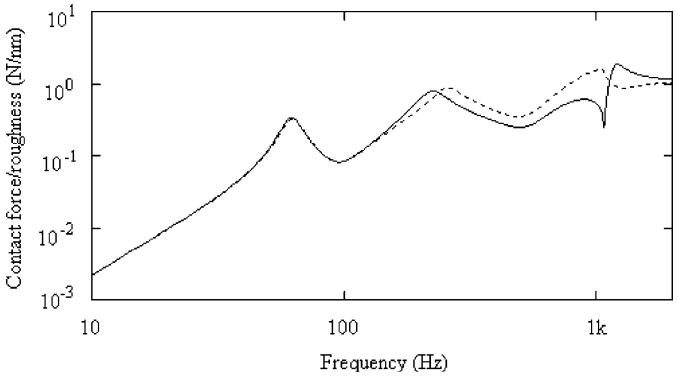

Fig. 16. Wheel/rail harmonic contact force: ———, between sleeper; and · · · · ·, above sleeper.

the rail's at frequencies below 60 Hz because the rail receptance is smaller in this domain. At higher frequencies though, the rail receptance is higher than the wheel's and the rail compensates the displacement of the system, caused by the roughness. The influence of the elastic Hertzian contact occurs in the pinned–pinned resonance/anti-resonance domain. The rail vibrates as a practical cord fixed at the sleepers. The following correlations occur in this frequency domain: the rail resonance determines the wheel anti-resonance and the rail

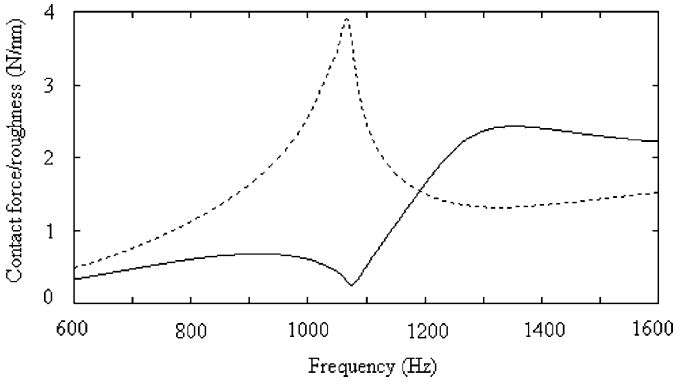

Fig. 17. Wheel/worn rail contact force (rigid contact): ———, between sleeper; and · · · · ·, above sleeper.

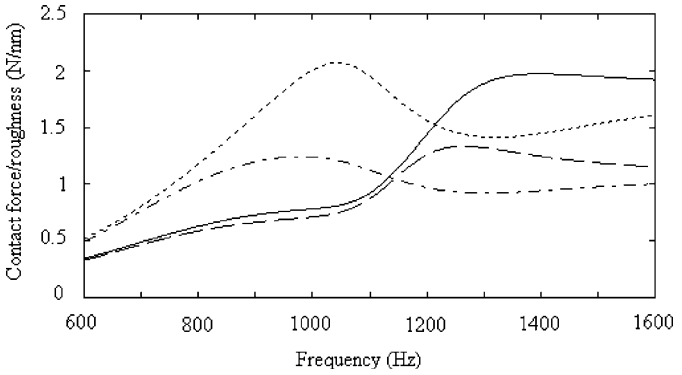

Fig. 18. The wheel/rail contact force for pinned–pinned inhibitive rail pad: ———, rigid contact between sleepers; · · · · ·, rigid contact above the sleeper; – – –, elastic contact between sleepers; and – · – · –, elastic contact above the sleeper.

anti-resonance leads to a local wheel resonance. Generally speaking, there are differences between the system's response above a sleeper and at mid span. These differences are maximal at the pinned–pinned resonance/anti-resonance, as shown in the contact force diagram.

The contact elasticity plays an important role in wheel/rail interaction at the pinned–pinned frequency. If the rail's profile is new, the contact elasticity is maximal and it partially compensates the pinned–pinned effect. In time though, the rail profile wears out and the contact elasticity decreases. The wheel/rail contact becomes rigid and cannot compensate the variations of rail elasticity between two sleepers anymore. As a result, a large variation of contact force along the span appears, as shown in Fig. 17. The contact stiffness k_H was considered as 1.837 GN/m. This aspect is significantly important in the occurrence and the development of the rail corrugation.

The rail pad is a strong damper for the rail foot's longitudinal displacement and rotation. If so, the rail bending wave is delayed and the pinned–pinned resonance is strongly damped. This compensates the 'loss of contact elasticity' effect. The contact force has a sensitively smaller variation between the two sleepers. Fig. 18 presents the wheel/rail contact force for a strong damping rail pad ($c_{rx} = 150\,\text{kN s/m}$, $c_{r\alpha} = 1.536\,\text{kN ms}$). This will be referred later as the *pinned–pinned inhibitive rail pad*. The presented diagram covers both, elastic and rigid wheel/rail contact. It is easy to observe that the *pinned–pinned inhibitive rail pad's* influence is smaller when we deal with an elastic contact. Its efficiency becomes obvious when we deal with a rigid contact.

5.2. Time-domain analysis

The previously presented track's Green matrix and wheel/rail interaction model were used for simulation purposes in the time-domain.

The track's Green matrix was determined for speed values of 24, 36, 48 and 60 m/s. The transitory T period for the numeric integration has been chosen according to the previous results as $T = 0.1$ s respectively, except for $V = 60$ m/s, for which $T = 0.08$ s.

The real part of the complex Green function was calculated for the resulting track length (VT) at a higher step (0.02 m), and then interpolated with spline functions at a 0.6 mm step. The time step for integrating the equations of motion varies between 10 and 25 μs. This domain is adequate for capturing the high-frequency dynamic responses of the wheel/rail system.

The temporal Green functions were calculated in a separate manner for each discrete point between the first and the second sleeper. The track's Green matrix was determined through temporal Green functions' assembly.

This wheel/rail model is used to simulate three dynamic cases: the steady-state interaction, wheel/rail rough interaction and wheel flat/rail interaction. In all these cases, at the initial moment, the wheel finds itself right above a sleeper, in a geometric contact (the contact force is null).

5.2.1. *Steady-state interaction*

It is assumed that the wheel and the rail are perfectly smooth and they have no defects. It is the situation in which the wheel/rail interaction is caused only by the parametric excitation of the track due to the varying dynamic stiffness of the discretely supported track. In other words, it is the ideal case of wheel/rail interaction, the so-called 'steady-state interaction' when the dynamic force is minimal.

Fig. 19 shows simulation results of the wheel/rail interaction—the steady-state interaction—when the wheel rolls on the track at a speed of 24 m/s. At the beginning, the wheel/rail system is in a transitory behaviour. During the transitory behaviour, the wheel and the rail are vibrating together at the system's first own frequency, which is about 60 Hz. After a period of approximately 0.15–0.20 s, the transitory behaviour fades away and the steady-state interaction begins. The transitory behaviour appears to be longer than the one of the numeric integration. In this particular case, it is about 0.1 s as mentioned above.

Fig. 20 presents the wheel/rail displacements at the contact point for the steady-state behaviour alongside the sleepers 25–30, for all simulated speeds. The wheel and rail displacements resemble. The wheel displacement is higher due to the elastic Hertzian contact. The minimal displacement of the wheel/rail system occurs above the sleepers at the speed of 24 m/s. At higher speeds, the minimal value occurs after the wheel has passed over the sleeper. Fig. 21 shows the wheel/rail contact force under the same conditions. The contact force is minimal above the sleeper. The effective contact force increases from 0.765 kN at 24 m/s to 3.24 kN at 36 m/s. At this speed, the frequency of passing over the sleepers equals the wheel/rail system's own frequency, and the effective contact force is maximal. At higher speeds, the effective force increases to 1.844 kN at 48 m/s and 1.91 kN at 60 m/s. The highest variations of the contact force occur close to the sleepers. This is caused by the variation of the dynamic stiffness of the rail due to the rail pad. This explains why the rail corrugation occurs firstly close to the sleepers. All the values involved are periodic because of the sleeper distancing effect.

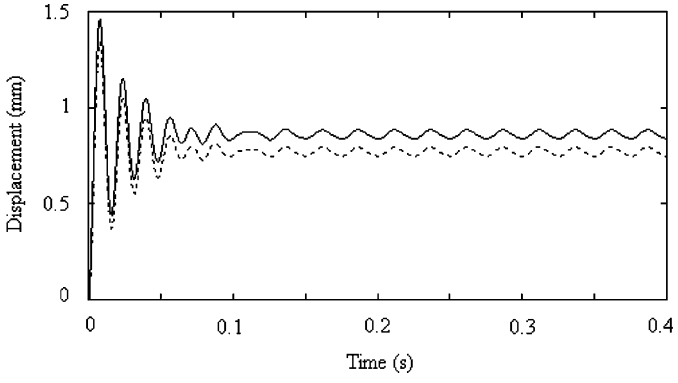

Fig. 19. Displacement of wheel and rail at the contact point in steady-state interaction, wheel speed $V = 24$ m/s: ———, wheel displacement; · · · · ·, rail displacement.

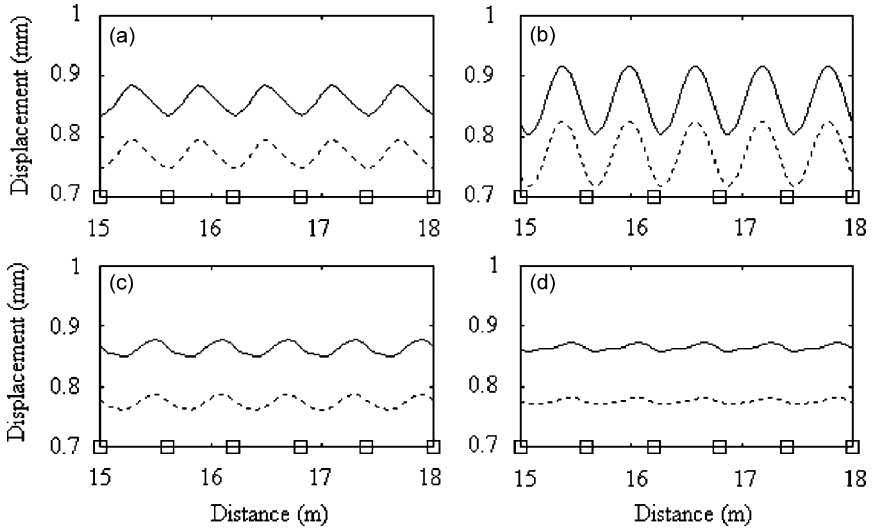

Fig. 20. Displacement of wheel and rail at the contact point in the steady-state interaction, at different speeds: (a) at 24 m/s; (b) at 36 m/s; (c) at 48 m/s; and (d) at 60 m/s; ———, wheel displacement; · · · · · ·, rail displacement; and □, sleeper position

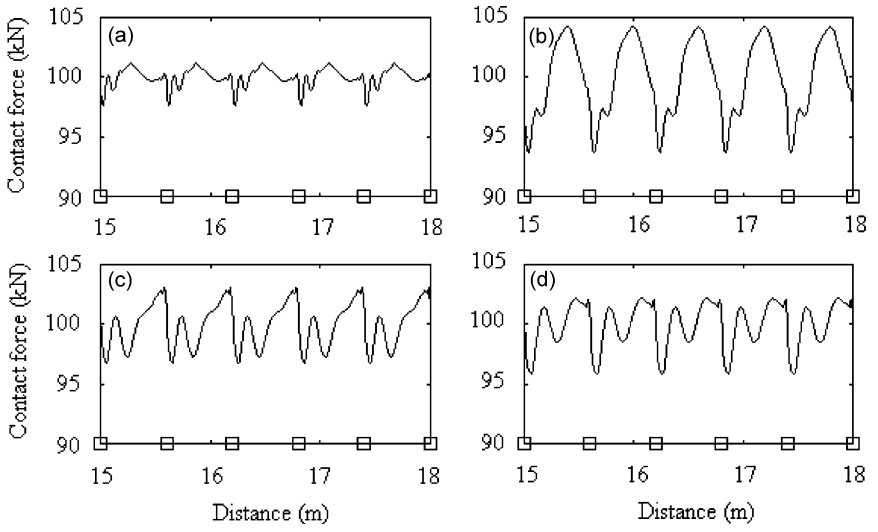

Fig. 21. Wheel/rail dynamic force in steady-state interaction at different speeds: (a) at 24 m/s; (b) at 36 m/s; (c) at 48 m/s; and (d) at 60 m/s; □, sleeper position.

Fig. 22 presents the contact force spectrum at the considered speeds for both, elastic and rigid wheel/rail contact. When dealing with a rigid contact, the Hertzian constant is considered as $C_H = 28.35 \times 10^{10}\,\mathrm{N/m^{3/2}}$. The spectra were calculated on a single period. First spectral component's frequency equals the ratio between the speed and the span length. The frequencies of the other spectral components are multiples of the fundamental frequency. The magnitude of the spectral components reaches its peak around 240 Hz, due to the second resonance of the wheel/rail system. A relative increase of the spectral components may be observed at the speeds of 24 and 36 m/s, especially around the pinned–pinned resonance frequency. The spectral components are higher in the pinned–pinned resonance frequency zone, when wedeal with a rigid contact. This is clear evidence of the contact stiffness' influence upon the wheel/rail interaction. The spectral components of the steady-state interaction influence the response spectrum when roughness is sinusoidal or random.

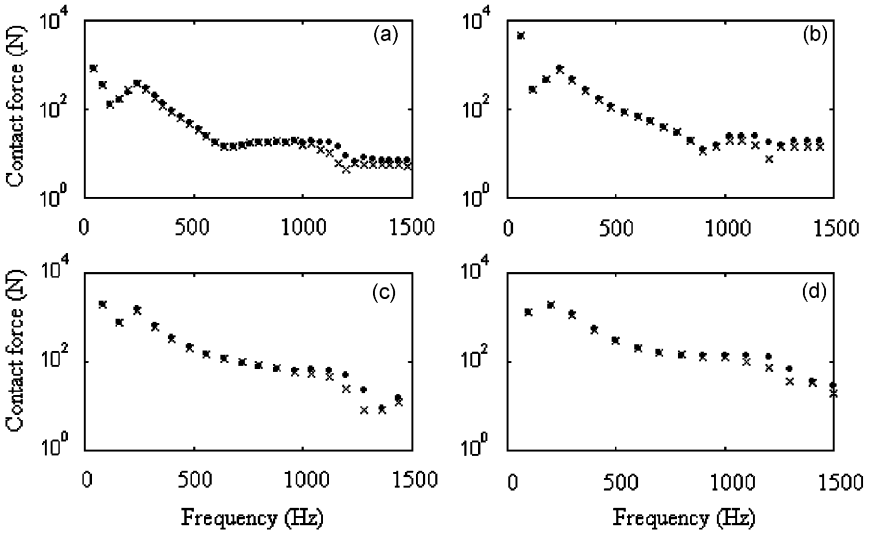

Fig. 22. Contact force spectra at different speeds: (a) at 24 m/s; (b) at 36 m/s; (c) at 48 m/s; and (d) at 60 m/s; ●, rigid contact; ×, elastic contact.

5.2.2. The corrugated rail

Rail corrugation is a specific rail defect consisting in the occurrence of certain waves on the rolling surface of the rail. The defect has many shapes but the rail corrugation of short wavelength, typically of 30–100 mm is the most dangerous one. Next, the case of a perfect round wheel which traverses a rail with a sinusoidal corrugation is presented. When rolling on a sinusoidal corrugated rail, the steady-state interaction is overlapped by the wheel/rail system's vibrations induced by the roughness. These last vibrations have a frequency equal to the ratio between the wheel's speed and the roughness' wavelength. The result is an amplitude-modulated vibration, in which the carrier frequency is caused by the sinusoidal roughness excitation and the modulation is given by the steady-state interaction.

Fig. 23 shows the result of the numeric simulation for a wheel moving at 60 m/s over a sinusoidal roughness which has a wavelength of 80 mm and the amplitude of 25 μm. The appropriate frequency for this roughness is $f_p = 750$ Hz and this is the carrier's frequency as well. The period of the periodic movement is 20 ms, which is the time for passing over two span lengths. The wheel amplitude is much smaller compared to the rail's amplitude at the considered contact point (Fig. 23a). This aspect is according with the results of the wheel/rail harmonic behaviour analysis. The sleeper displacement is smaller than the rail's, as the rail pad's 'filter' effect is obvious (Fig. 23b).

The character of modulated vibration is best illustrated by the time dependence of the wheel/rail contact force. The spectrum of the contact force has two kinds of components: the steady-state interaction components and the modulation effect-added components. The modulation effect refers to the fact that the carrier frequency modulates the steady-state interaction components. The fundamental component of the steady-state interaction has a $f_0 = 100$ Hz frequency. The other harmonics have frequencies equal to integer multiples of the fundamental frequency. The resulted modulated spectral components have frequencies equal to $f_p \pm kf_0$ where k stands for an integer number.

If the carrier's frequency is an integer multiple of the previously defined fundamental frequency, both kinds of components will overlap. Fig. 24 shows the results for a simulation that considers a wheel rolling at 60 m/s over a sinusoidal roughness which has wavelengths of 50 and 60 mm and amplitudes of 8 and 12 μm, respectively. In this particular case, there are two different carriers by the frequencies of 1200 and 1000 Hz. The period of this periodic movement equals the time for passing from a sleeper to another, which is about 10 ms. The amplitude of wheel displacement is smaller than the rail's at the considered contact point. The wheel/rail contact force varies between 58.36 and 139.30 kN. The effective force has a value of 15.77 kN. The spectrum has two peaks corresponding to the carrier frequencies. The spectra of the two dynamic contact

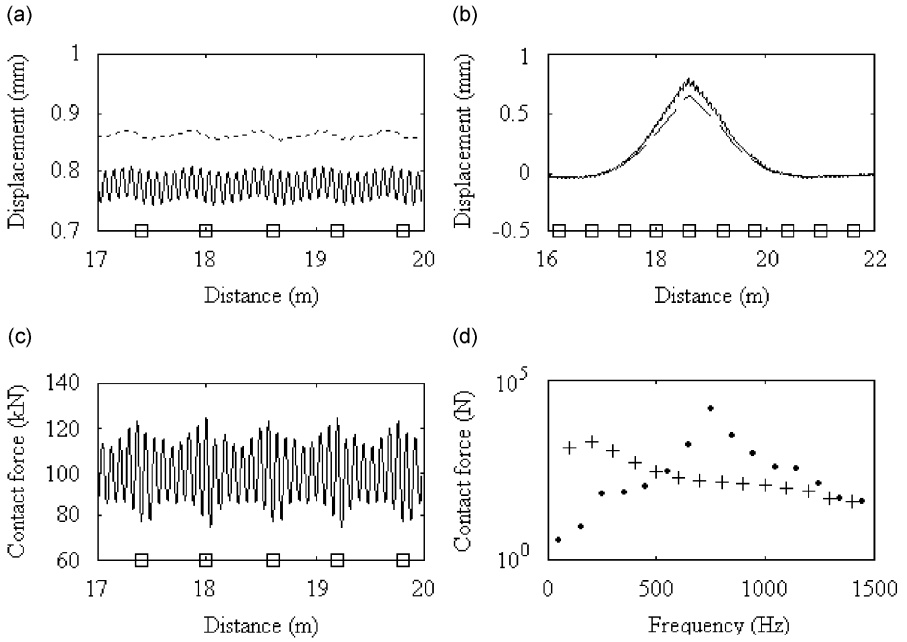

Fig. 23. The wheel/track response due to harmonic excitation by the wavelength of 80 mm, wheel speed $V = 60$ m/s: (a) · · · · ·, wheel displacement, ———, rail displacement at contact point; □, sleeper position; (b) ——, rail displacement above sleeper # 32 at 18.6 m, – – –, the displacement of the sleeper # 32; (c) contact force; and (d) contact force spectrum, ×, steady-state interaction components, ●, modulated components.

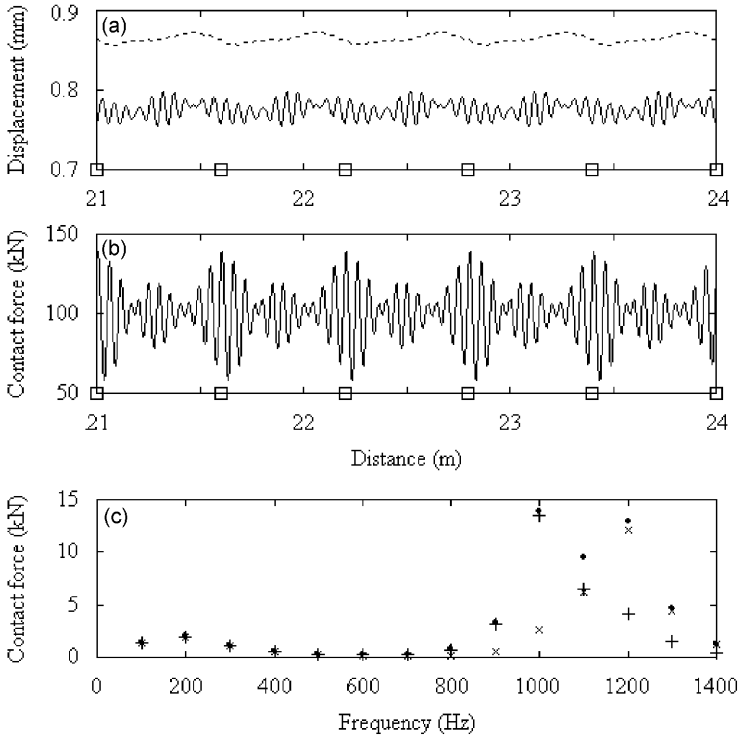

Fig. 24. The results for a simulation that considers a wheel rolling at 60 m/s over a sinusoidal roughness which has wavelengths of 50 and 60 mm and amplitudes of 8 and 12 μm: (a) · · · · ·, wheel displacement ———, rail displacement at contact point; (b) contact force; and (c) contact force spectrum: ●, for both wavelength; +, for wavelength of 60 mm only; ×, for wavelength of 50 mm only.

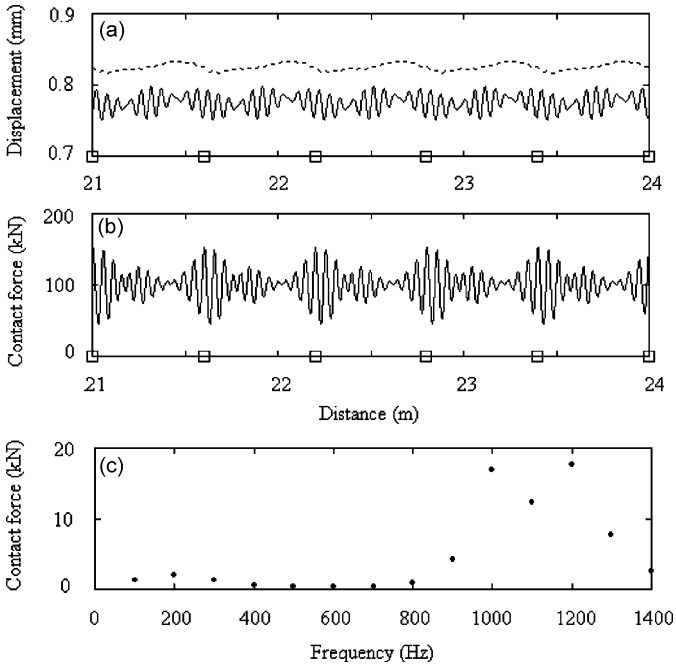

Fig. 25. Wheel/worn rail response due to two harmonic excitation with wavelength of 50 and 60 mm, wheel speed $V = 60$ m/s: (a) · · · · ·, wheel displacement, ———, rail displacement at contact point; (b) contact force; and (c) contact force spectrum.

forces corresponding to the roughness are presented as well. It is easy to notice the overlapping effect especially on the 1100 Hz component.

When dealing with a rigid contact, the appropriate results are shown in Fig. 25. The vibratory behaviour is much more intense. The wheel/rail contact force varies between 44.78 and 152.04 kN and has the effective value of 20.52 kN. The components of the force spectrum are obviously higher than the ones of the elastic contact. Those at frequencies above 800 Hz are at least 25% higher.

Fig. 26 shows the simulation results for the *pinned–pinned inhibitive rail pad* ($c_{rx} = 150$ kN s/m, $c_{r\alpha} = 1.536$ kN ms), under the same conditions. The contact force varies between 64.51 and 133.48 kN for elastic contact, having its effective value of 13.74 kN. If a wheel is rolled on a corrugated rail (rigid contact), the contact force varies from 54.59 to 143.59 kN and has an effective value of 16.69 kN. The comparative spectral analysis of the wheel/rail contact force shows that the high-damping rail pad is efficient at frequencies above 700 Hz.

5.2.3. *The wheel flat/rail interaction*

The flat is a serious damage of the rolling surface of the railway wheel. This defect occurs when the wheel is blocked due to a braking system malfunction. When a wheel having a flat defect rolls on the rail, a periodic impact force occurs at the contact point, producing impact noise.

The issue of simulating this kind of impact may be solved using the presented model. A new flat has a cord shape located on the circumference of the wheel's longitudinal section. Anyway, after a very short period of time, the edges of a flat profile become rounded due to the wear.

The wheel flat/rail interaction may be studied considering a perfectly round wheel rolling on a rail which presents an indentation on its head. For this particular purpose, an indentation situated on the rail head is considered. It has the following equation [24]:

$$z_r = \frac{e}{2}\left(1 - \cos 2\pi \frac{x}{l}\right),$$

where e stands for the thickness of the flat and l stands for its length.

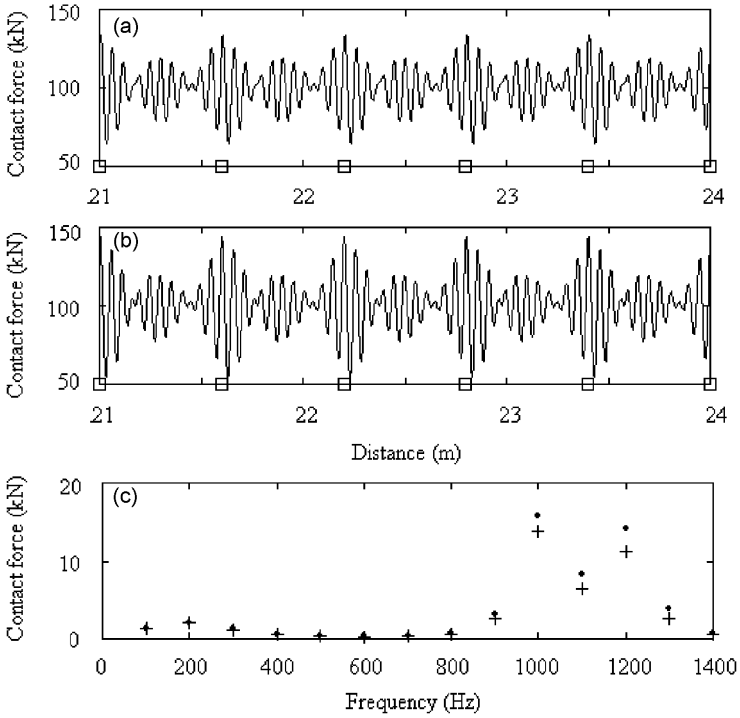

Fig. 26. Wheel/rail supported on pinned–pinned inhibitive rail pad interaction force due to two harmonic excitation with wavelength of 50 and 60 mm, wheel speed $V = 60$ m/s: (a) elastic contact; (b) rigid contact; (c) contact force spectrum: +, elastic contact, ●, rigid contact.

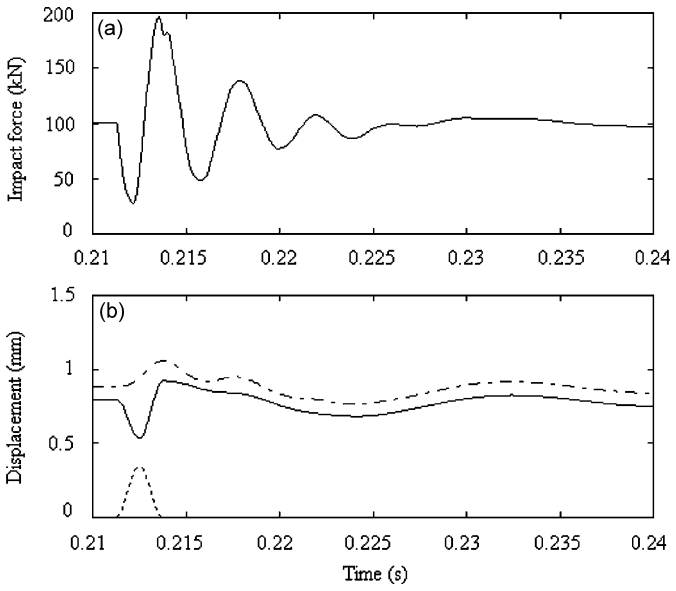

Fig. 27. Wheel/rail response due to a 0.35 mm deep and 60 mm length wheel flat between sleeper at wheel speed 24 m/s: (a) impact force; (b) – · – · –, wheel displacement; ———, rail displacement at contact point; and · · · · ·, rail head indentation.

Fig. 27 shows the results of the simulated wheel flat/rail interaction at 24 m/s at mid span. The length of the flat is 60 mm and its maximal depth is 0.35 mm. When the wheel rolls over the indentation on the rail head, it cannot immediately follow the indentation due to their inertia. The relative distance between the wheel and rail head increases and the contact force is partially unloaded. This trend is maintained until the wheel reaches

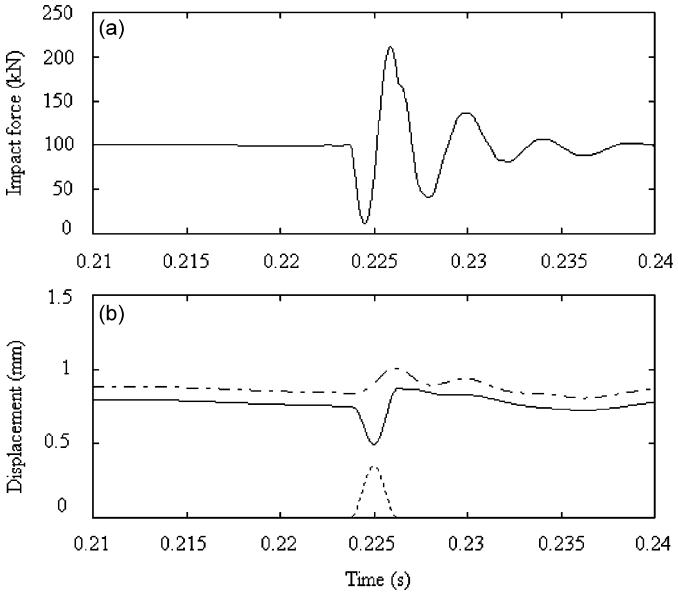

Fig. 28. Wheel/rail response due to a 0.35 mm deep and 60 mm length wheel flat above the sleeper at wheel speed 24 m/s: (a) impact force; (b) – · – · –, wheel displacement; ———, rail displacement at contact point; and · · · · ·, rail head indentation.

approximately above the maximum of the flat equivalent excitation. During this time, the rail is pushed upwards by the ballast's and rail pad's reaction and the wheel is pushed downwards by the steady force which becomes higher than the contact force. As a consequence of these opposing movements, the wheel/rail impact occurs. The contact force reaches a spectacular value of 196.5 kN when the wheel passes the rail head indentation. Shortly after the impact, the motion is quickly damped. If the flat zone is right above a sleeper, the impact is just a little more violent, as Fig. 28 shows. The maximal impact force is 211 kN.

The higher the speed, the more violent the impact force. Fig. 29 shows the result of the numeric simulation for the same flat zone, impacting at mid span at 60 m/s. This time, the contact is lost for about 0.41 ms. The impact force has a tremendous magnitude of 320 kN.

If the flat zone is longer, the wheel might lose contact even twice. For e.g., Fig. 30 shows the wheel/rail interaction for a wheel having a flat zone of 120 and 1.5 mm indentation. The speed is 24 m/s and an elastic contact is considered. The system's evolution resembles, except that now the wheel loses contact twice. First, the wheel loses contact for 2.1 ms, then passes the rail head indentation and loses contact again for 1.6 ms. The first impact lasts for 2.775 ms and has a magnitude of 401.9 kN and the second has a much smaller magnitude of 215.2 kN.

The rail pad damping leads to a reduction of rail receptance for pinned–pinned frequencies-the rail becomes more rigid. Despite this, the influence on the impact is very poor, even for rigid contact. Fig. 31 presents the impact force above a sleeper, for worn rail with regular rail pad and *pinned–pinned inhibitive rail pad*. There are very little differences. The magnitude of the impact force slightly increases from 221.3 kN (regular rail pad) to 222.5 kN (*pinned–pinned inhibitive rail pad*).

6. Conclusions

The wheel/rail interaction and the response to various vertical excitations were studied using a mixed 'Timoshenko beam/infinite bar on a discrete pad' model. A complex model for the rail pad was proposed: two translations and one rotation—in order to simulate the conditions for stopping the bending wave's propagation. The issue of time-domain analysis for wheel/rail interaction was solved using the real Green functions method. These were calculated by integrating the complex Green functions. The track's Green matrix was determined using the properties of the Green functions. The Green matrix was helpful to simulate

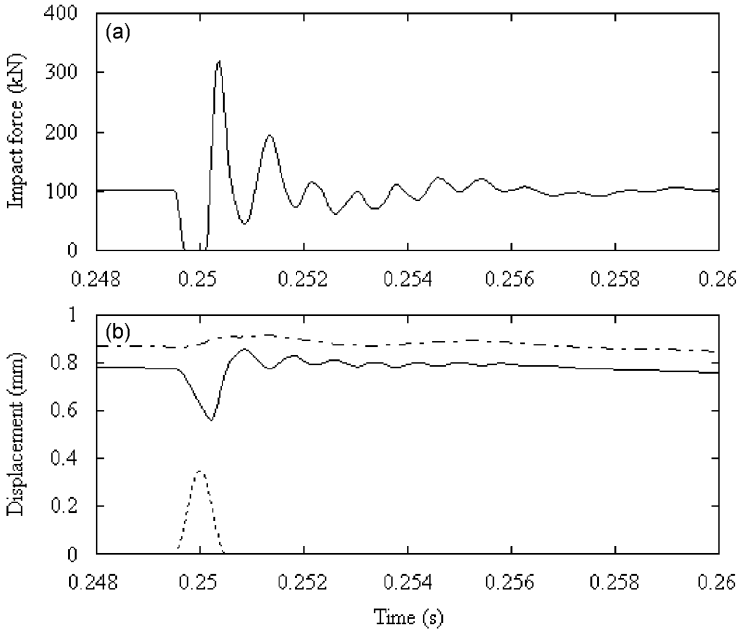

Fig. 29. Wheel/rail response due to a 0.35 mm deep and 60 mm length wheel flat above the sleeper at wheel speed 60 m/s: (a) impact force; (b) – · – · –, wheel displacement; ———, rail displacement at contact point; and · · · · ·, rail head indentation.

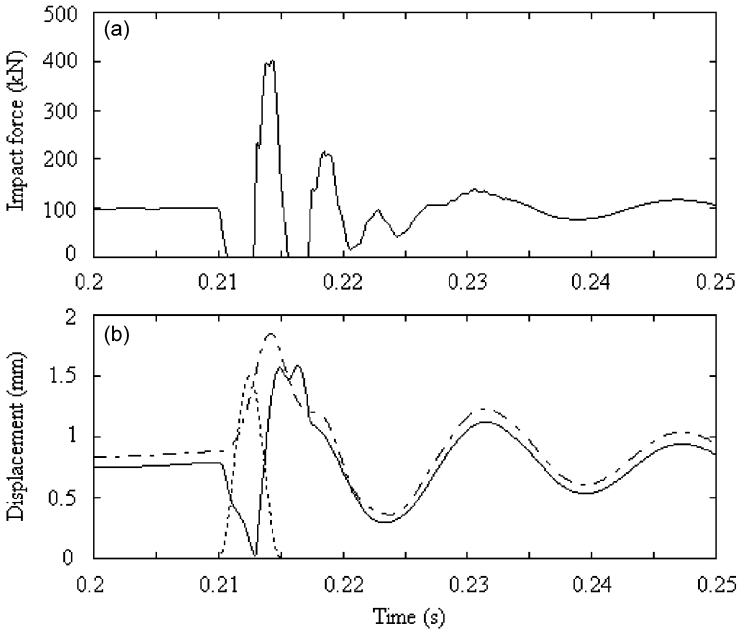

Fig. 30. Wheel/rail response due to a 1.5 mm deep and 120 mm length wheel flat above the sleeper at wheel speed 24 m/s: (a) impact force; (b) – · – · –, wheel displacement; ———, rail displacement at contact point; and · · · · ·, rail head indentation.

the wheel/rail interaction for any distance and for any type of vertical excitation. For this, a mass wheel model was combined with the track model.

The steady-state interaction is influenced mainly by the running speed and by the wheel/rail system's own low frequency. The wheel/rail contact force has a peak corresponding to the speed for which the frequency of

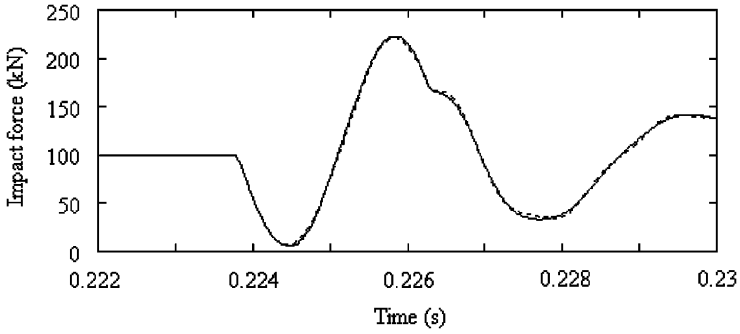

Fig. 31. Comparison of the wheel flat/rail on regular rail pad interaction with the wheel flat/rail on pinned–pinned inhibitive rail pad interaction due to a 0.35 mm deep and 60 mm length wheel flat above the sleeper at wheel speed 24 m/s: ———, pinned–pinned inhibitive rail pad; and · · · · ·, regular rail pad.

passing over the sleepers equals the first resonance frequency of the wheel/rail system. At higher speeds, the contact force increases respectively. The contact force spectrum contains many harmonics because of the variation of rail's receptance between the two sleepers. The fundamental frequency of the force spectrum equals the frequency of passing over sleepers. The spectral components are higher at the resonance frequencies of the wheel/rail system.

As the rail head wear progresses, the wheel/rail contact becomes more rigid. The variation of the contact force increases in the steady-state interaction.

If the wheel rolls on a corrugated rail, the wheel/rail contact force becomes amplitude modulated, and the carrier's frequency equals the frequency of passing over corrugation. The spectral components may be overlapped especially in the pinned–pinned frequency domain.

The contact force has wide variation if the contact is rigid. This aspect leads to corrugation development. Numeric simulations revealed that the use of a damping improved rail pad (pinned–pinned inhibitive rail pad) reduces the amplitude of the contact force.

The wheel flat/rail interaction is dominated by the impact force due to the shock which occurs when the wheel passes over the flat zone and it is pushed downwards by the dead load and the rail is pushed upwards by the track's reaction. In addition to that, the impact force is slightly stronger above the sleeper than in the middle of the sleeper bay. The magnitude of the impact force depends on the flat size and on the running speed. The contact stiffness and the pinned–pinned inhibitive rail pad have a very marginal influence.

Appendix A

The differential matrix operators from the Eqs. (1) and (2) are:

$$\mathbf{L}_{x,t}=\begin{bmatrix} ES\dfrac{\partial^2}{\partial x^2}-m\dfrac{\partial^2}{\partial t^2} & 0 & 0 \\ 0 & GS\kappa\dfrac{\partial^2}{\partial x^2}-m\dfrac{\partial^2}{\partial t^2} & -GS\kappa\dfrac{\partial}{\partial x} \\ 0 & GS\kappa\dfrac{\partial}{\partial x} & EI\dfrac{\partial^2}{\partial x^2}-GS\kappa-\rho I\dfrac{\partial^2}{\partial t^2} \end{bmatrix},$$

$$\mathbf{A}_t=\begin{bmatrix} -c_{rx}\dfrac{\mathrm{d}}{\mathrm{d}t}-k_{rx} & 0 & h\left(c_{rx}\dfrac{\mathrm{d}}{\mathrm{d}t}+k_{rx}\right) \\ 0 & -c_{rz}\dfrac{\mathrm{d}}{\mathrm{d}t}-k_{rz} & 0 \\ h\left(c_{rx}\dfrac{\mathrm{d}}{\mathrm{d}t}+k_{rx}\right) & 0 & -(c_{r\alpha}+h^2c_{rx})\dfrac{\mathrm{d}}{\mathrm{d}t}-k_{r\alpha}-h^2k_{rx} \end{bmatrix},$$

$$\mathbf{B}_t = \begin{bmatrix} c_{rx}\frac{\mathrm{d}}{\mathrm{d}t} + k_{rx} & 0 & h_1\left(c_{rx}\frac{\mathrm{d}}{\mathrm{d}t} + k_{rx}\right) \\ 0 & c_{rz}\frac{\mathrm{d}}{\mathrm{d}t} + k_{rz} & 0 \\ -h\left(c_{rx}\frac{\mathrm{d}}{\mathrm{d}t} + k_{rx}\right) & 0 & (c_{r\alpha} - hh_1c_{rx})\frac{\mathrm{d}}{\mathrm{d}t} + k_{r\alpha} - hh_1k_{rx} \end{bmatrix},$$

$$\mathbf{C}_t = \begin{bmatrix} M_s\frac{\mathrm{d}^2}{\mathrm{d}t^2} + c_{sx}\frac{\mathrm{d}}{\mathrm{d}t} + k_{sx} & 0 & \Delta c\frac{\mathrm{d}}{\mathrm{d}t} + \Delta k \\ 0 & M_s\frac{\mathrm{d}^2}{\mathrm{d}t^2} + c_{sz}\frac{\mathrm{d}}{\mathrm{d}t} + k_{sz} & 0 \\ \Delta c\frac{\mathrm{d}}{\mathrm{d}t} + \Delta k & 0 & I_s\frac{\mathrm{d}^2}{\mathrm{d}t^2} + c_{s\alpha}\frac{\mathrm{d}}{\mathrm{d}t} + k_{s\alpha} \end{bmatrix},$$

with

$$c_{sx} = c_{rx} + c_{bx}, \quad c_{sz} = c_{rz} + c_{bz}, \quad c_{s\alpha} = c_{r\alpha} + h_1^2c_{rx} + h_2^2c_{bx}, \quad \Delta c = h_1c_{rx} - h_2c_{bx},$$

$$k_{sx} = k_{rx} + k_{bx}, \quad k_{sz} = k_{rz} + k_{bz}, \quad k_{s\alpha} = k_{r\alpha} + h_1^2k_{rx} + h_2^2k_{bx}, \quad \Delta k = h_1k_{rx} - h_2k_{bx},$$

and

$$\mathbf{D}_t = \begin{bmatrix} c_{rx}\frac{\mathrm{d}}{\mathrm{d}t} + k_{rx} & 0 & -h\left(c_{rx}\frac{\mathrm{d}}{\mathrm{d}t} + k_{rx}\right) \\ 0 & c_{rz}\frac{\mathrm{d}}{\mathrm{d}t} + k_{rz} & 0 \\ h_1\left(c_{rx}\frac{\mathrm{d}}{\mathrm{d}t} + k_{rx}\right) & 0 & (c_{r\alpha} - hh_1c_{rx})\frac{\mathrm{d}}{\mathrm{d}t} + k_{r\alpha} - hh_1k_{rx} \end{bmatrix}.$$

References

[1] J.P. Remington, Wheel/rail noise—Part I: characterization of the wheel/rail dynamic system, *Journal of Sound and Vibration* 46 (1976) 359–379.

[2] D.J. Thompson, Wheel/rail contact noise: development and detailed evaluation of a theoretical model for the generation of wheel and rail vibration due to surface roughness. *ORE DT* 204 (C 163), Utrecht, 1988.

[3] Y. Sato, Study on high-frequency in track operated with high-speed trains, *Quarterly Reports of RTRI* 18 (1977) 109–114.

[4] S.L. Grassie, R.W. Gregory, D. Harrison, K.L. Johnson, The dynamic response of railway track to high frequency vertical excitation, *Journal Mechanical Engineering Science* 24 (1982) 77–90.

[5] P.J. Remington, Wheel/rail noise I: theoretical analysis, *Journal of the Acoustical Society of America* 81 (1987) 1805–1023.

[6] D.J. Thompson, Wheel–rail noise generation, Part I: introduction and interaction model, *Journal of Sound and Vibration* 161 (1993) 387–400.

[7] R.A. Clark, P.A. Dean, J.A. Elkins, S.G. Newton, An investigation into the dynamic effects of railway vehicles running on corrugated rails, *Journal Mechanical Engineering Science* 24 (1982) 65–76.

[8] J.C.O. Nielsen, A. Igeland, Vertical dynamic interaction between train and track—influence of wheel and track imperfections, *Journal of Sound and Vibration* 185 (1995) 825–839.

[9] K. Hou, J. Kalousek, R. Dong, A dynamic model for an asymmetrical vehicle/track system, *Journal of Sound and Vibration* 267 (2003) 591–604.

[10] R.G. Dong, Vertical Dynamics of Railway Vehicle-track System, PhD Thesis, Concordia University, 1994.

[11] T.X. Wu, D.J. Thompson, On the parametric excitation of the wheel/track system, *Journal of Sound and Vibration* 278 (2004) 725–747.

[12] T. Krzyzynski, K. Popp, On the travelling wave approach for discrete-continuous structures under moving loads, *ZAMM Zeitschrift fur Angewadte Mathematik und Mechanik* 76 (Suppl. 4) (1996) 149–152.

[13] T. Krzyzynski, On dynamics of a railway track modelled as a two-dimension periodic structure, *Heavy Vehicle Systems* 6 (1) (1999) 330–344.

[14] G. Degrande, D. Clouteau, R. Othman, M. Arnst, H. Chebli, R. Klein, P. Chatterjee, B. Janssens, A numerical model for ground-borne vibrations from underground railway traffic based on a periodic finite element-boundary element formulation, *Journal of Sound and Vibration* 293 (3–5) (2006) 645–666.
[15] D. Clouteau, G. Degrande, G. Lombaert, Numerical modelling of traffic induced vibrations, *Meccanica* 36 (4) (2001) 401–420.
[16] P.M. Belotserkovskiy, On the oscillations of infinite periodic beams subjected to a moving concentrated force, *Journal of Sound and Vibration* 193 (3) (1996) 705–712.
[17] A.V. Metrikine, A.L. Bosch, Dynamic response of a two-level catenary to a moving load, *Journal of Sound and Vibration* 292 (2006) 676–693.
[18] A.V. Metrikine, K. Popp, Vibration of periodically supported beam on an elastic half-space, *European Journal of Mechanics A—Solids* 18 (4) (1999) 679–701.
[19] T.X. Wu, D.J. Thompson, A double Timoshenko beam model for vertical analysis of railway track at high frequencies, *Journal of Sound and Vibration* 224 (1999) 329–348.
[20] A. Nordborg, Wheel/rail noise generation due to nonlinear effects and parametric excitation, *Journal of the Acoustical Society of America* 111 (2002) 1772–1781.
[21] Tr. Mazilu, Propagation of harmonic vertical waves in a rail, *Scientific Bulletin Series D: Mechanical Engineering* 67 (2) (2005) 99–110.
[22] D.J. Thompson, B. Hemsworth, N. Vincent, Experimental validation of the TWINS prediction program for rolling noise, Part 1: description of the model and method, *Journal of Sound and Vibration* 193 (1996) 123–135.
[23] D.J. Thompson, Wheel–rail noise generation, part III: rail vibration, *Journal of Sound and Vibration* 161 (1993) 421–446.
[24] T.X. Wu, D.J. Thompson, A hybrid model for the noise generation due to railway wheel flats, *Journal of Sound and Vibration* 251 (2002) 115–139.